TECHNISCHE UNIVERSITÄT MÜNCHEN

WALTHER-MEISSNER-INSTITUT FÜR TIEFTEMPERATUR-FORSCHUNG

BAYERISCHE AKADEMIE DER WISSENSCHAFTEN

Superconducting spintronics with magnetic insulators

Master's thesis

Yuhao Sun

Advisor: Prof. Dr. Rudolf Gross

Supervisor: Dr. Matthias Althammer

Garching – February 1, 2023

Contents

1 Introduction

The digital revolution in the late half of the 20th century has changed our lives significantly. Central to this revolution is the mass production and widespread use of digital logic devices based on complementary metal-oxide semiconductors. Widespread use of digital logic, MOSFETs (MOS transistors), integrated circuit chips, and their derived technologies, including computers, microprocessors, digital cellular phones, and the Internet change daily lives totally. One example is the way we store our information. In the late 1980s, less than 1% of the world's technologically stored information was in digital format, while it was 94% in 2007, with more than 99% by 2014 [1]. Furthermore, the Fourth Industrial Revolution with the trend towards automation and data exchange in manufacturing technologies and processes which include cyber-physical systems, industrial internet of things, cloud computing, cognitive computing, and artificial intelligence, are on their way [2]. Therefore, there will be a high demand for logic devices with higher performance in the near future. But the logic devices based on CMOS suffer from overheating problems due to their low energy efficiency. The famous Moore's law [3], which the development of CMOS-based devices obeys, seems to come to an end [4]. An appropriate alternative for data storage and processing becomes ever more pressing due to the high demand for computing devices with high performance. One auspicious step in this direction is represented by spintronics research. Spintronics offers the potential for creating circuits in which logic operations controlled by spin currents can be performed faster and with greater energy efficiency than the charge-based equivalent in semiconductor transistor technologies [5]. A key requirement for spintronics is that the signals from the spintronics are large enough to detect which requires the spin degree of freedom to relax slowly enough. Hence, trying to prolong spin lifetimes in materials is one of the most important goals in spintronics. A combination of spintronics and superconductivity can resolve this problem. The results look promising: spin-polarized quasiparticles injected into superconductors have been shown to have spin lifetimes that exceed those of spin-polarized quasiparticles in normal metals by several orders of magnitude [6, 7].

In this thesis, we focus on the quasiparticles (QP) mediated spin transport at the interface between a superconductor (SC) and a ferrimagnetic insulator (FMI). We generate a spin current perpendicular to the SC/FMI interface via the spin Seebeck effect (SSE) [8, 9] and convert it into a voltage signal via the inverse spin Hall effect (iSHE) [10, 11] in the superconductor. We perform our experiments on a three-terminal spin transport device fabricated on a yttrium iron garnet (YIG) thin film, allowing for two different temperature gradients. The devices consist of two platinum (Pt) strips acting as a side heater and a reference detector, and a superconducting niobium nitride (NbN) strip in the center, acting as the detector of thermopower signals. On the top of the superconducting NbN strip, we pattern a heater structure. We can control the sign and magnitude of the temperature gradient at the FMI/SC interface by using either the top heater or the side heater. We pattern the structure using e-beam lithography technology and deposit the material via magnetron sputtering deposition in the Superbowl sputtering system. To detect the thermopower signals, we perform so-called angle dependence magnetoresistance (ADMR) measurements in a superconducting magnet liquid helium cryostat. In our measurements, we apply heat-

ing currents I_{inj} at one of the heaters and measure the corresponding thermopower signal at different temperatures around T_c in a superconductor when rotating the orientation of the external magnetic field in three orthogonal rotation planes. Furthermore, we use the 2^{nd} harmonic lock-in technique to detect the thermopower voltage signals by a sinusoidal modulation fo I_{inj}. According to a recent report by Jeon et al.[6], a large SSE signal, which can be greatly enhanced by up to three orders of magnitude compared with that in the normal state, is expected to be detected around T_c. Interestingly, apart from the enhancement of the thermopower signals, we find rich behaviors of thermopower signals around T_c, including a shift in angle position, a large offset, and several sign changes of the signal. Moreover, we also detect an ADMR around T_c in a three-terminal device fabricated on a silicon substrate.

The thesis is structured as follows: We first introduce some essential theories in Ch.2, including the inverse spin Hall effect, the spin Seebeck effect, and the spin currents in the superconductor. Then, in Ch.3, we introduce the fabrication details and the technique we use to investigate the SSE. Furthermore, we present our experimental results in Ch.4. Finally, the summary and outlook are presented in Ch.5.

2 Theoretical concepts

In this chapter, we introduce the spin transport process at the SC/FMI interface from the theoretical side. The spin transport process at the SC/FMI interface consists of the following components: (a) The spin accumulation in the FMI layer: The FMI layer serves as the reservoir of the injected spins. In this thesis, the spins are carried by the thermal-induced magnons in the YIG layer. The corresponding spin polarization is determined by the orientation of the magnetization and can be controlled by the external magnetic field. (b) The driving force of the spin current: The spin currents are driven by the temperature difference between the YIG layer and the superconductor layer via the SSE. (c) The spin transport in SC: The spin current is carried mainly by quasi particles (Qp) in the SC/FMI heterostructure near T_c. (d) The detection of spin current: The spin current is converted into charge current via the ISHE and detected as a voltage signal in the open circuit. Therefore in this chapter, we first introduce the basic concept of spin current generation via the spin Hall effect (SHE) [10] and the detection via inverse spin hall effect (iSHE) [11] in Sec.2.1. Furthermore, we introduce the generation of thermal spin currents via the spin Seebeck effect (SSE) [8, 12] which is a spin-motive force generated by a temperature gradient in Sec.2.2. Finally, we describe the quasiparticle (QP) mediated spin transport at SC/FMI interface [13, 14], in Sec.2.3.

2.1 Spin Current

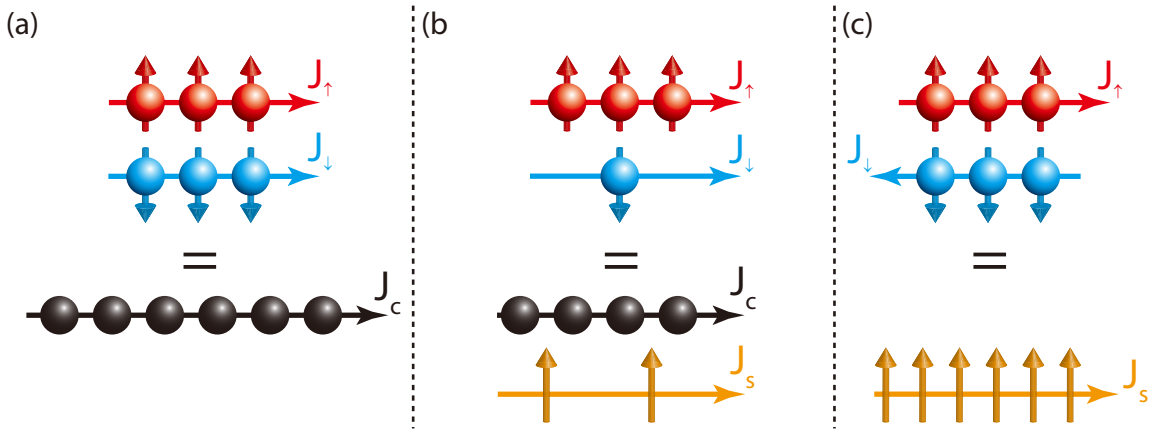

Figure 2.1: (a) The charge current with the same number ↑ and ↓ spins: there exist no spin transport in this charge current; (b) The charge current with different numbers of ↑ and ↓ spins: Spin current appears along the charge current; (c) Electrons with different spins move into the opposit directions; There exist no charge current but pure spin current. Figure adapted from [15].

We briefly introduce the charge-spin inter-conversion processes of electrons in this section. We first introduce the basic concept of the spin current and several ways to generate spin currents. (a) The first one is the generation of spin-polarized carriers. We should try to polarize all spin carriers along the same direction, such as totally ↑ or totally down ↓. If these spin-polarized carriers are driven to move in the same direction by a gradient such as eg. a temperature gradient, we observe a transport of spin/a spin current. (b) Another way is to create an imbalance of the carriers with spin ↑ and ↓. Therefore, there exist a different

number of a spin ↑ and a spin ↓ and we obtain a spin transport in total. (c) Finally, the last way is to make the carriers with spin ↑ and spin ↓ travel in opposite directions, so that we can get a spin transport without a net movement of the carriers. These processes are illustrated in Fig.2.1. Taking the spins carried by electrons as an example. A single electron can be in two spin states: one is the spin-up ↑ and the other is spin-down ↓. The charge current can be written via a two-current model:

$$J_{\mathrm{c}} = J_{\uparrow} + J_{\downarrow} \tag{1}$$

The subscripts here denote the electron spin polarization s pointing up (↑) or down (↓). Therefore, the spin transport or the spin current of this charge current can be written as

$$J_{\mathrm{s}} = -\frac{\hbar}{2e}(J_{\uparrow} - J_{\downarrow}) \tag{2}$$

where $q = -e < 0$ is the charge of the electron and $\hbar$ is the reduced Planck constant. For charge currents in a conducting ferromagnet, it is a good example of situation (b). The spin splitting is caused by the exhange interaction of the ferromagnetic, wich cause the a different density of states at the Fermi level for spin up (↑) and spin down (↓) electrons. Therefore, a charge current in a conducting ferromagnet leads to the spin current given by Eq.(2). The conversion of the spin currents into the charge currents in this thesis is via the inverse spin Hall effect, which is a spin-dependent scattering due to the spin-orbit coupling.

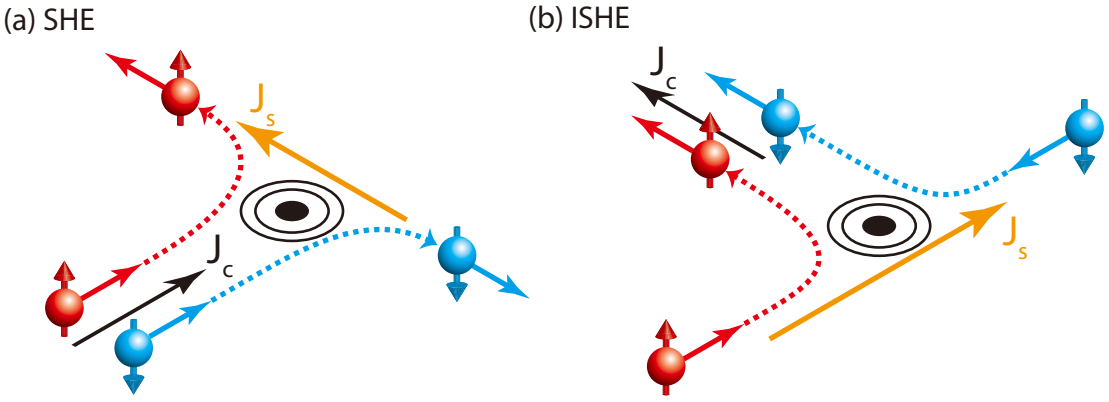

Figure 2.2: Illustration of the spin Hall effect and the inverse spin Hall effect. (a) Spin Hall effect: conversion from the charge current J_{c} to the spin current J_{s} due to the spin-dependent scattering; (b) Inverse spin Hall effect: conversion from the spin current J_{s} to the charge current J_{c}. Figure adapted from [15].

The spin Hall effect[10] is a transport phenomenon consisting of the spin accumulation on the lateral surfaces of a sample induced by an applied charge current. The opposite surface boundaries will have spins of opposite signs. It is analogous to the classical Hall effect, where charges of opposite signs appear on the opposing lateral surfaces in a conducting sample in a magnetic field. In the case of the classical Hall effect, the charges accumulating at the boundaries are in compensation for the Lorentz force acting on the charge carriers in the sample due to the external magnetic field. No magnetic field is needed for the spin Hall effect which is a purely spin-based phenomenon. The spin Hall effect is a spin transport phenomenon due to the different behaviors of the scattering process of the charges

with different spins. In conductors with strong spin-orbit coupling, electrons with different spin angular momentum are scattered in opposite directions. Therefore, the transport of a charge current gives rise to a transverse spin current. The relation between a charge current and a spin current is [10]

$$J_{\mathrm{s}}^{\mathrm{SHE}} = \Theta_{\mathrm{SH}} \frac{\hbar}{2e} J_c \times s \tag{3}$$

Here Θ_{SH} is the spin Hall angle, which characterizes the conversion efficiency between charge currents and spin currents [10] is. Moreover, the inverse process of this phenomenon is called the inverse spin Hall effect [10, 11]. Due to the fact that there are no methods to detect spin current directly, we can take advantage of the inverse spin Hall effect (iSHE) to detect the spin current. The conversion from a spin current to a charge current is given by

$$J_{\mathrm{c}}^{\mathrm{iSHE}} = \Theta_{\mathrm{SH}} \frac{\hbar}{2e} J_s \times s \tag{4}$$

The spin Hall angle Θ_{SH}, which parameterizes the efficiency of the spin-charge conversations, is governed by both intrinsic effects from the band structure[16] and extrinsic effects from the scattering of electrons with defects of the material [17, 18]. In order to get large charge currents that can be easily detected, a material with a large strong spin-orbit coupling is needed. Since the spin-orbit coupling strength is proportional to the atomic number as Z^4, heavy metals such as platinum (Pt) [19–22] or tantalum (Ta) [23, 24] are materials of choice.

2.2 Spin Seebeck Effect (SSE)

Here, we briefly introduce the concept of the spin current and how the spin transport with a charge current. Then we introduce the spin current driven by an external temperature gradient, which is called the spin Seebeck effect (SSE). Also similar to the conversion of temperature differences and charge current, known as the Peltier–Seebeck effect, a spin current is generated along the direction of the external temperature gradient. One of the most interesting cases of the SSE is the SSE at the interface of a magnetic order insulator (MOI) and a normal metal(NM). Because of the fact that a charge current cannot transmit at the MOI/NM interface, we can generate a pure spin current driven by a thermal gradient. Up to now, a number of studies demonstrated the SSE at the interface of a platinum(Pt) layer and a yttrium iron garnet (YIG) layer in great detail [9, 12, 25–33], where the YIG layer is the source of the polarized spin and the Pt is a good detector due to its large spin Hall angle Θ_{SH}. Therefore, we take the SSE at the Pt/YIG interface as an example. According to widely accepted theories [8, 12, 34–36], the spin transport arises from the temperature difference $\Delta T_{\mathrm{me}} = T_{\mathrm{m}} - T_{\mathrm{e}}$ of the temperature T_{m} of the magnonic subsystem in the YIG layer and the temperature T_{e} of the electronic subsystem in the Pt layer. The magnitude of the spin current J_{s} is proportional to the temperature difference ΔT_{me} at the interface.

As the orientation of spin carriers does not change via the SSE, the SSE only contributes to the movement of the spin carriers. The spin carriers are spin-polarized at the Pt/YIG interface via spin-flip scattering. The orientation of the spin polarization s of the spin current is governed by the magnetization orientation M of the YIG layer. Due to the fact that

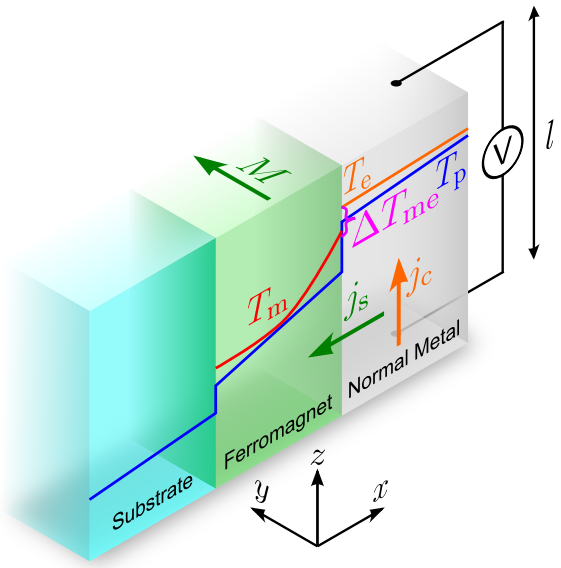

Figure 2.3: A illustration of the spin Seebeck effect. The temperature difference ΔT_{me} between the temperature of spin carriers in ferromagnets (magnons) and normal metal(electrons) give rises to a spin current j_{s} perpendicular to the interface. Then this spin current j_{s} is converted to a charge current $j_c \propto j_s \times s$, where s is the polarization of the spin current. Figure adapted from [37].

the iSHE is dependent on the orientation of the spin polarization s of the spin current, the detected SSE signals are dependent on the magnetization orientation M of the YIG layer. As the conversion of the spin current and the charge current via iSHE follows the relation $j_c \propto j_s \times s$ from Eq.(4), The SSE voltage obeys a $\cos(\alpha)$ dependence (in which α is the angle of magnetization with respect to the Pt strip). When the orientation of the magnetization is parallel to the pt strip ($\alpha = 0°$), we expect to detect the maximal signal. Moreover, when the orientation of the magnetization is perpendicular or anti-perpendicular to the Pt strip, we expect to detect no signals from the Pt. For the SSE at the SC/FMI interface, things become more complicated. The spin carriers in the superconductor are the spin-triplet Cooper pairs or QPs. The iSHE in the SC obeys the the same charge-spin conversion principles and angular dependence on the orientation of the magnetization. But we expect in addition temperature dependence, which will be discussed in the next section.

In this thesis, the magnitude and direction of temperature gradients are controlled by the magnitude of charge current I_{inj} applied on either the top heater or the side heater. We take advantage of the Joule heating of the heater to generate the temperature gradient. Hence, the temperature difference ΔT_{me} is proportional to the temperature increase due to the Joule heating of the heater, and it is therefore proportional to the electric heating power P_{JH}. In this thesis, we use sinusoidal AC currents to generate the temperature gradient. Thus, $P_{\mathrm{JH}} = \frac{1}{2} R I_{\mathrm{inj}}^2$, in which R is the electric resistance of the heater. We expect a quadratic dependence of the SSE on the injection current ($V_{\mathrm{SSE}} \propto I_{\mathrm{inj}}^2$).

2.3 Spin transport at the FMI/SC interface

In this thesis, we focus on spin transport at the FMI/SC interface. The spin is injected into the SC layer from the FMI layer via SSE and is detected via the iSHE in the superconductor.

However, compared to spin transport experiments at the FMI/NM interface [8, 12, 34–36], spin transports are mediated with the quasiparticles (QP) in SC instead of normal electrons. Therefore, charge and spin imbalances may have different characteristic length scales due to spin-charge separation [38–40]. Moreover, thermally excited QPs in SC can carry a spin current over long distances, as spin excitations in SCs have long lifetimes [41–46], so the QP-mediated spin Hall effect is expected to be enhanced markedly [13, 47–49].

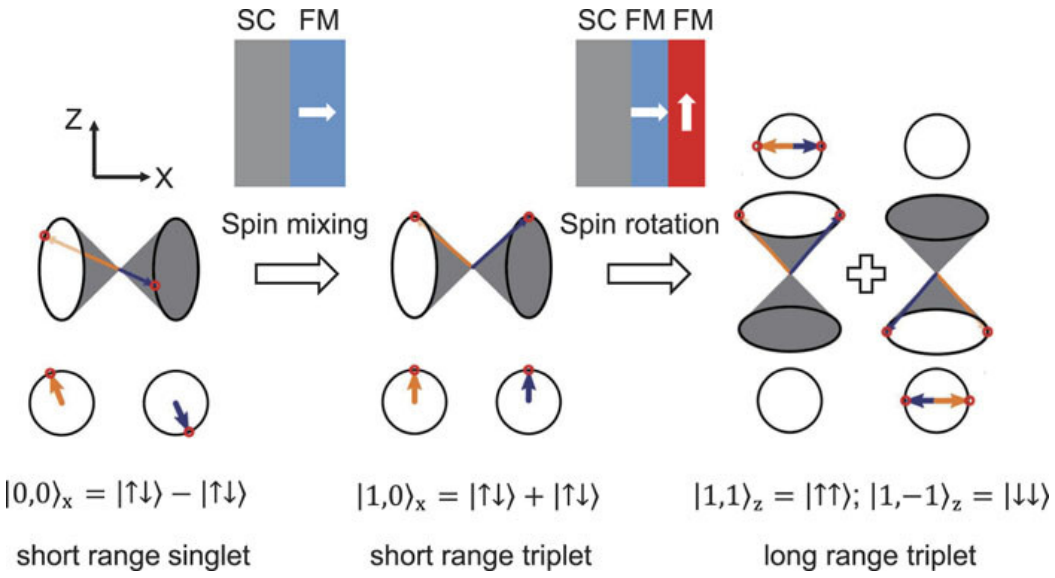

Figure 2.4: Cooper pair conversion between spin-singlet and spin-triplet states at SC/FM interface: Spin-mixing at the SC/FM interface shifts the spin-dependent phase of electrons in a singlet state, generating zero-spin triplet pair correlations. A second interface with a misaligned magnetization leads to spin rotation and generates equal-spin triplet Cooper pairs. Figure adapted from [50].

For electrons, spin lifetimes are nevertheless typically fairly short in diffusive materials owing to spin-orbit and spin-flip scattering processes which leads to spin randomization. Another major hurdle relates to the fact that, because electrons carry spin and charge, they are susceptible to processes that cause dissipation and decoherence due to the charge degree of freedom. Copper pairs in the superconductor with a net spin component exhibit smaller scattering rates from processes involving spin-orbit impurities [41–46]. Therefore, the spin lifetime of QPs in SC can be increased by many orders of magnitude relative to results in ferromagnetic metals, which will give rise to the greatly enhanced ISHE signal.

Although Cooper pairs in SC are expected to exhibit a long spin lifetime, there is an obstacle to spin-polarize the Cooper pairs in the SC. The charge current in the SC is carried by the Cooper pairs consisting of two interacting electrons due to the BCS theory [51]. A Cooper pair can be seen as a two-electron system, where the two electrons reside in a spin-singlet antisymmetric state ($|\uparrow\downarrow\rangle - |\downarrow\uparrow\rangle$). The spin-singlet state with a spin of quantum number $s = 0$ only has one allowed value of the spin component $m_s = 0$, so it can not be spin polarized. But according to the Pauli principle, the spin part of Cooper pairs does not necessarily have to be in a spin-singlet state. The Cooper pairs can also reside in a spin-triplet state which is symmetric under fermion exchange - that is, ($|\uparrow\downarrow\rangle + |\downarrow\uparrow\rangle$), $|\uparrow\uparrow\rangle$ or $|\downarrow\downarrow\rangle$ [52, 53]. Different from the spin-singlet state, the spin-triplet state with a spin of quantum number $s = 1$ has three allowed values of the spin component $m_s = -1, 0, +1$, but

only the states with the spin component $m_s = \pm 1$ can be spin polarized. In the presence of a magnetic field, the Zeeman interaction between spins and a magnetic field favors a parallel alignment, meaning that a strong enough magnetic field can break the Cooper pairs. Therefore, only the Cooper pairs in $|\uparrow\uparrow\rangle$ and $|\downarrow\downarrow\rangle$ states coexist with a magnetic field as the Zeeman interaction will not break such Cooper pairs. For triplet-state, as the Cooper pairs can be spin-polarized, the spin-triplet supercurrents can carry a net spin component.

The spin-singlet Cooper pairs can be converted into the spin-triplet Cooper pairs via spin mixing and spin rotation at the SC/FMI interface [47, 50, 54], shown in Fig.2.4. Via the spin-mixing, a spin singlet Cooper pair ($|\uparrow\downarrow\rangle - |\downarrow\uparrow\rangle$) is converted into a short-range spin-triplet Cooper pair ($|\uparrow\downarrow\rangle + |\downarrow\uparrow\rangle$). The spin-mixing the process generates the $S_z = 0$ triplet component from a spin-singlet source through spin-dependent phase shifts that the electrons experience when propagating through a ferromagnetic region or when scattered at a ferromagnetic interface. Via the spin-rotation, we get the long-range spin-triplet Cooper pairs ($|\uparrow\uparrow\rangle$, $|\downarrow\downarrow\rangle$). When the magnetization of the system is textured such that the spin-quantization axis varies spatially, the effect of spin rotation comes into play, thus causing the different spin-triplet components to transform into each other [5]. In this thesis, we patterned a superconducting NbN strip (SC) on a YIG substrate (FMI) to generate the spin-triplet Cooper pairs.

Finally, we introduce the QP-mediated spin-charge conversion in a superconductor, which is the SHE and iSHE of QPs in a superconductor [7, 13, 55]. According to the theory [13, 14], quasiparticle spin currents injected from an FMI layer into an SC layer create charge currents in the transverse direction by the iSHE and accumulate spin and charge near the side edges of a superconductor. Moreover, the density of QPs has a maximum below the transition temperature, so we expect an enhancement of SSE signals related to QP below the critical temperature of the SC.

3 Experimental Details

In this chapter, we introduce some experimental details which are necessary for the comprehension of the results presented in the following chapters. First, the three strips structure allowing for two different temperature gradients, generated by a top heater or a side heater, is introduced in Ch 3.1. Then the fabrication procedure and the material system are presented in Ch 3.2, as well as the experimental setup and measurements techniques in Ch 3.3.

3.1 Structure and material

In this section, we introduce the layout of the three-terminal devices for the detection of the SSE investigated in experiments including the functionality of its individual components as well as the base materials. Furthermore, we discuss some experimental drawbacks of the layout.

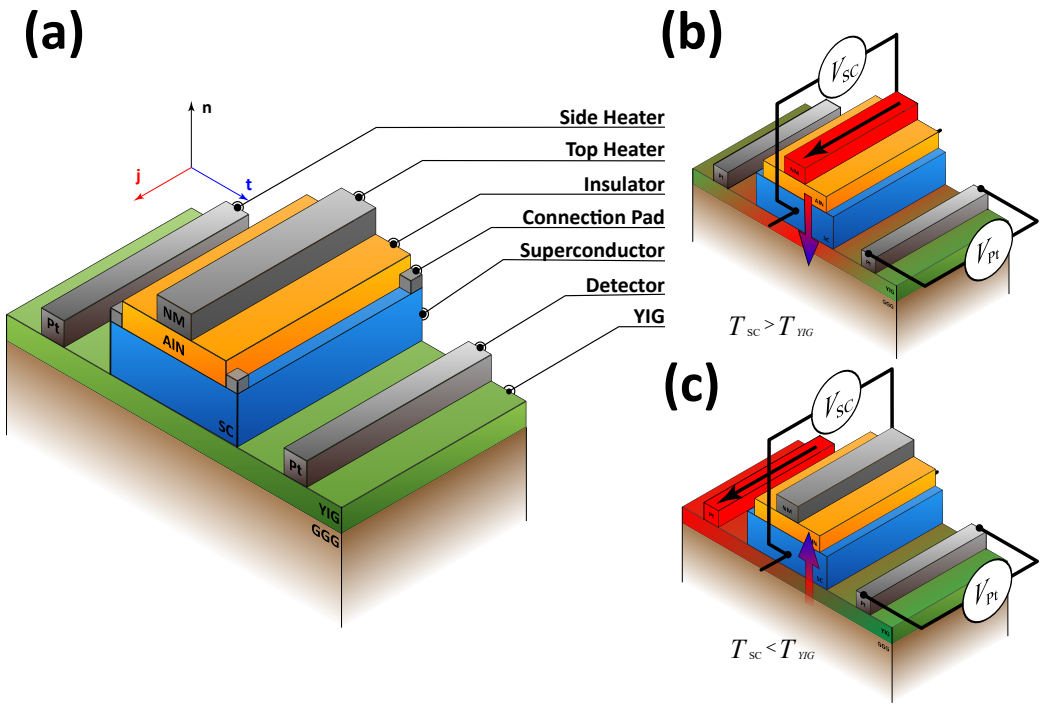

Figure 3.1: Experiment structure with a top heater and a side heater: (a) The three-terminal devices are fabricated on an LPE-YIG substrate grown on a GGG substrate consisting of a side heater, superconductor, insulator, top heater, reference detector, and connection pads. (b) The temperature gradient at the FMI/SC interface when driving the top heater ($T_{\mathrm{SC}} > T_{\mathrm{YIG}}$). (c) Temperature when driving the side heater ($T_{\mathrm{SC}} < T_{\mathrm{YIG}}$).

Function In order to investigate thermal spin transportations across the FMI/SC interface, a three-terminal device capable of generating a controllable temperature gradient across the FMI/SC interface is needed. To this end, we design a three-terminal device with outer heaters and a top heater. The structure fabricated on a yttrium iron garnet (YIG) substrate consists of two $80\,\mu\mathrm{m} \times 0.5\,\mu\mathrm{m} \times 5\,\mathrm{nm}$ platinum strips working as a side heater and reference detector, and a $100\,\mu\mathrm{m} \times 6\,\mu\mathrm{m}$ niobium nitride (NbN) stripe in the middle

with variable thicknesses of (12, 17 or 22) nm. On top, we pattern a $100\mu m \times 0.5\mu m$ platinum strip heater on top insulated by a 35 nm aluminum nitride (AlN) layer. First, we will illustrate the operation principle in Fig 3.1.

As is shown in Fig 3.1, we can control the sign and magnitude of the temperature gradient at the FMI/SC interface by using either the top heater or one of the side heaters. When we drive a charge current through the side heater, it will heat the FMI layer and raise the temperature of the YIG layer T_{YIG} above that of the superconductor layer T_{SC}. Conversely, when we drive a charge current through the top heater, we can generate a temperature gradient with the opposite sign at the interface ($T_{\mathrm{SC}} > T_{\mathrm{YIG}}$). Moreover, as the non-local spin Seebeck effect on platinum is well studied experimentally [9, 12, 25–33], the additional platinum stripe can work as a reference. In Fig 3.2, we sketch the sample layout and list the used materials in Tab 3.1.

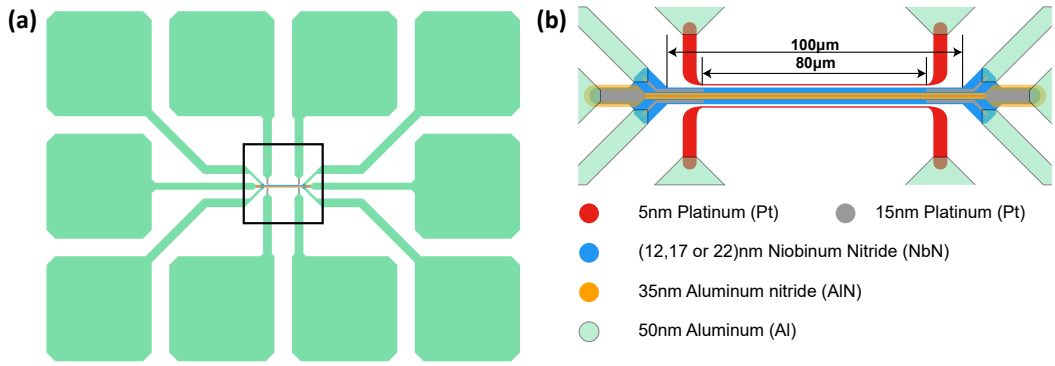

Figure 3.2: Layout and material system: (a) the whole layout of the structure including the outer connection pads; (b) The layout of the core part and the material system.

steps	Function	Material	Length(µm)	Width(µm)	Thickness(nm)
1	Superconductor	NbN	100	6	12, 17, 22
2	Side heater/detector	Pt	80	0.5	5
3	Insulator	AlN	-	3	35
4	Top heater	Pt	-	0.5	15
4	Small connection needle	Pt	-	1	15
5	Connection pads	Al	-	-	50

Table 3.1: Geometry and materials used for our devices.

Material In the following, used materials for individual parts of the device are introduced. For the choice of material, we have to consider the material, which has to meet the requirements to perform the desired functionality under our experimental conditions.

Magnetic insulator (YIG) We investigate the transport of thermal spin currents from the FMI layer to the SC layer. The magnetic insulator is the source of thermal magnons. The thermal magnons are generated by heating and accumulate in the magnetic insulator layer. The magnetic insulator layer should hence be good for the generation, accumulation, and transport of magnons to generate large thermal spin currents. The Gilbert damping parameter α, the thickness, and the surface roughness of the material need to be taken into account in the material choice. We use a 2µm thick yttrium iron garnet (YIG) film

grown via liquid phase epitaxy (LPE) on ta gadolinium gallium garnet (GGG) substrate as the magnetic insulator. Due to its low Gilbert damping parameter $\alpha \simeq 10^{-5}$, spin waves can propagate over long distances. Furthermore, there are a number of works on the spin transport in a Pt/YIG heterostructure that serve as references to our experiments [9, 12, 25–33]. As the YIG layer also serves as the base layer of the structure, surface roughness is also an important parameter in our experiment.

Superconductor (NbN) The superconducting layer serves as a detector of the SSE signal. Magnons, which transmit the YIG/SC interface, will be converted into electrical signals in the superconductor due to the inverse spin Hall effect [10, 11]. Hence, we have to account for the superconducting transition temperature T_c, which has to be experimentally accessible by the available liquid helium flow cryostat. Furthermore, the superconducting coherence length is a relevant parameter as it is the length scale at which superconducting proximity effects, such as the quasiparticle spin Hall effect, can manifest [6]. As the YIG layer is not a good substrate for the deposition of the superconductor, we require robust superconductors with a high T_c. We use a $100\mu\mathrm{m} \times 6\mu\mathrm{m}$ niobium nitride stripe with different thicknesses (12nm, 17nm, and 22nm) as the superconductor. Niobium nitride (NbN) is a compound of niobium and nitrogen with the chemical formula NbN, and it is a type-II superconducting material, with a critical transition temperature of about $16\,\mathrm{K}$. In our initial experiments, we used elementary Niobium, which is expected to have a longer coherence length of about 30nm [6], But the low T_c of about 2K in these devices was too low for our experiments.

Side heater/Detector (Pt) The side heater is used to generate the temperature gradient and the detector is responsible for the detection of the SSE signal across the YIG layer. The desired material should hence have a high resistivity to generate heat, good chemical stability to allow for high heating currents, and a large spin hall angle Θ_{SH} to get large inverse spin Hall signals. We use an $80\ \mu\mathrm{m} \times 0.5\mu\mathrm{m} \times 5\mathrm{nm}$ platinum strip as the side heater and detector due to its large spin Hall angle of about $\Theta_{\mathrm{SH}} = 0.1$, as illustrated in Sec.2.1. The side heater and the reference detector are the same in material and size, and have the same distance to the middle superconductor. Hence, they are interchangeable in our experiments. Platinum, with the symbol Pt, is a widely used heavy metal in spin transport experiments.

Insulator (AlN) The insulating layer is meant to electrically insulate the top heater and superconductor or connection pad when driving the heating current on the top heater and transfer heat from the top heater to the superconductor. The insulating layer needs to be electrically insulating, but conduct a heat current to the top Pt detector. Under the condition of sufficient electrical insulation, the insulator should be as thin as possible to generate a large temperature gradient. We use a $35\,\mathrm{nm}$ thick aluminum nitride (AlN) layer as the insulator. Aluminum nitride is a solid nitride of aluminum [56].

Top heater (Pt) The top heater will only act as a heater, so it only needs high resistivity and stability. For the choice of thickness, we should consider the roughness of the

insulator(AlN) surface.

Connection Pad (Pt/Al) The connection pad is used to connect our outer devices. The connection pads have two parts. The first part is the detection layer on the top of the superconductor, which is used to detect the accumulated charge at the surface of the superconductor. To achieve good insulation, the thickness of this layer is thinner than the insulator layer. We use a $15\,\mathrm{nm}$ Pt layer which is deposited with the top heater at the same time, in order to reduce the number of lithography steps. The other part is the connection pads used for bonding. We should use soft and stable materials with high electrical conductivity to make a good connection to the main structure. To this end, we use a $50\,\mathrm{nm}$ thick aluminum layer for the connection pad.

Discussion By patterning an additional heater structure on top of the NbN strip to create different temperature gradients, there are several potential problems that need to be taken into account. First, we should consider the influence of the heater structure on top. Due to the additional fabrication step, the heater structure on top may reduce the properties of the superconductor, such as critical temperature and width of the superconducting transition. The other part we should take into account is the influence of the additional interface on the spin transport process. The new insulator/superconductor interface might affect the thermal spin transport process in the superconductor, and thereby affect the detected voltage signal. Another point of discussion is the influence of the transverse temperature gradient generated by the side heaters. As is shown in Fig 3.2, the width of the middle superconductor is much larger than the top and side heater, so we expect a lateral temperature gradient at the interface. Moreover, different heaters will generate different transverse temperature gradients. The side heater generates an asymmetric temperature gradient in which one side is hot and the other side is cold, while the top heater will generate a symmetric lateral temperature gradient. However, as the superconducting layer is not a good heat conductor, the latter case can be neglected.

3.2 Fabrication

In this section, we present the detailed fabrication process and introduce the used experimental technique. Our fabrication process consists of three parts, which are sample preparation, the lithography process, and sputtering deposition.

Preparation For the preparation of the chips, we first perform a cleaning procedure with Piranha acid to remove residual organic compounds. Piranha solution is a mixture of sulfuric acid and hydrogen peroxide, used to clean organic residues off substrates.

E-Beam Lithography Electron beam lithography, like photolithography, is a general term used for techniques that uses a focused electron beam to produce a minutely patterned resist layer over a substrate to protect selected areas of it during subsequent etching and deposition operations. The layout will be transferred into an e-beam resist spin-coated on

the substrate. The chemical structure of the e-beam resist is chemically altered underexposure and is consequently removed via the corresponding developer leaving the resist only in the unexposed area of the film.

After preparation, we sequentially deposit the structure in the order of marker, superconductor, side strip, insulator, top heater/connection, and large connection pads, as listed in Tab 3.1. To fabricate the structure into the desired shape, we will use the electron beam lithography via the so-called lift-off technique, which involves spin coating (coat substrate with electron beam resist), writing (exposing the resist film with an electron beam), developing (wash away the exposed parts), depositing (deposit the material via sputter deposition) and lift-off (wash away the resist layer). The $50\,\mathrm{nm}$ platinum markers fabricated in the first step are used in the writing process for an alignment of the subsequent lithography steps.

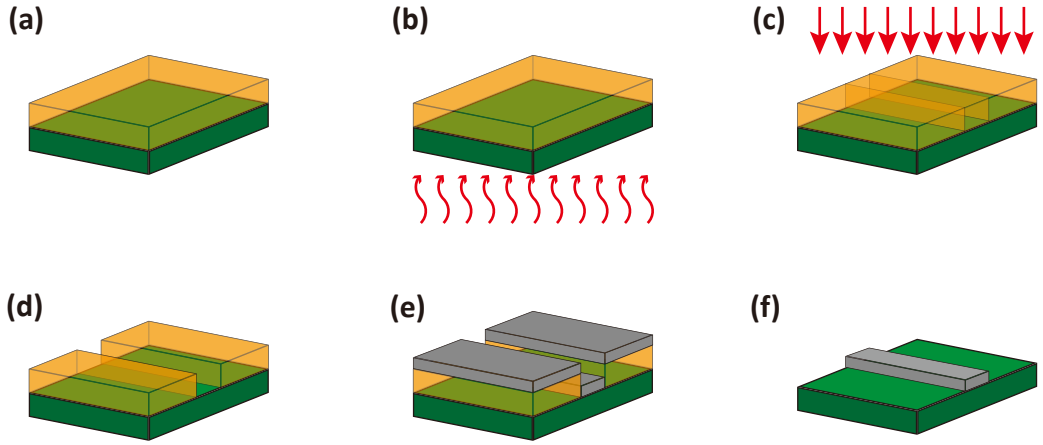

Figure 3.3: General lift-off process (a) The sample is covered with resist. (b) Resist bake-out; (c) E-beam exposure; (d) Resist development; (e) Sputter deposition of a metallic thin film; (f) Lift-off process: The resist is removed by rinsing the sample in solvents.

Resist	Volume	Spin-coating	Bake out	Developer	Remover
PMMA 600K	10µL	1 min@4000rpm	5min@170°C	AR600-56, 120s	AR600-71
PMMA 950K					
Electra-92	20µL	1 min@4000rpm	2min@90°C		H_2O

Table 3.2: All resists used for coating, including resist volume, spin coating parameter, bake out parameter, development time, and the corresponding remover for lift-off.

1. **Spin-coating**: In the coating process, we use a two-layer PMMA e-beam resist system for a high-resolution lift-off. In detail, we use *PMMA 650K* as the bottom layer, *PMMA 950K* as the top layer, and *Electra 92* as a conductive resist layer as for electron beam lithography on an insulating substrate, a conductive top layer (*Electra 92*) is needed to avoid charging effects on the substrate. Before coating the substrate, we clean the substrate. The chips are cleaned with acetone and isopropanol (IPA) in an ultrasonic bath. We will use a high ultrasonic bath power ("*9*" in the lab condition) only at the first step and a low ultrasonic bath power ("*1*" in the lab condition) in the following steps to avoid damaging the structures on the sample surface. Chips will

be blow-dried with nitrogen gas to protect the surface after cleaning. Next, we will fabricate the double-layer resist system layer by layer. We will pipette the resist solution on the substrate ($10\,\mu L$ for PMMA600K/950K and $20\,\mu L$ for *Electra-92*) and chips are rotated with a spin coater at 4000rpm speed for $1\,\mathrm{min}$ to obtain a resist layer with a homogeneous layer thickness. To remove the solvents, the resist is then hard-baked on a hotplate. For PMMA 650k and PMMA 950K, chips will be baked for $5\,\mathrm{min}$ at $170\,^{\circ}\mathrm{C}$ each and the *Electra-92* is baked for $2\,\mathrm{min}$ at $90\,^{\circ}\mathrm{C}$. In the first fabrication step for the makers, we drop some gold particles at the edge of chips before we spincoat the *Electra-92* layer. As there are no markers on the substrate in the first step, the gold particles allow focus on the substrate surface markers for focus. After all three resist layers are coated, the chips are ready for e-beam exposure.

2. **Writing**: The chips are installed into the *NanoBeam nB5* e-beam system lithography system (*NanoBeam Ltd.*) for exposure. To precisely expose the desired area, we use markers to determine the position and focus the beam on the surface of the chips. The markers are patterned into $10\mu\mathrm{m} \times 10\mu\mathrm{m}$ squares made of platinum. The detailed writing process is introduced in Appendix A.1.

3. **Development**: After the e-beam exposure, we will remove the exposed parts of the resist with the suitable developing solvent. First, the top conductive layer is removed with distilled water. Then the chips are put into the developing solution (*AR 600-56*) for $2\,\mathrm{min}$ to remove the exposed area. Finally, we use IPA to stop the removal process.

4. **Deposition** Materials are deposited via magnetron sputtering deposition in the Superbowl sputtering system. The principle of the sputtering process is introduced later.

5. **Lift-off**: As the material is deposited both on the resist layer and substrate, upon removal of the resist layer via solvents, the material on top will also be removed, leaving only the desired structures on the substrate. The resist layer is removed with the solution, *AR 600-71*, and acetone. After lift-off, the chip is cleaned carefully with acetone and IPA in an ultrasonic bath to get rid of the possible residue and resist and be ready for further fabrication.

This is the general fabrication process for one layer. The structure will be fabricated layer by layer with the same process.

Sputtering Sputtering is a phenomenon, in which microscopic particles of solid material are ejected from its surface after the material is itself bombarded by energetic particles of plasma or gas. The principle of sputtering is that energetic ions are accelerated toward the target material and collide with atoms of a target material. Due to the exchange of momentum between energetic ions and atoms in the target material, the first collision leads to more collisions inside the target resulting in a collision cascade, and the collisions inside the material lead to secondary electrons and surface atoms, which make the atoms inside the target leave the surface. The atoms can then diffuse to the sample placed above the target. There are several ways to realize such a sputtering process like ion-beam sputtering

and reactive sputtering. In this work, only DC-magnetron sputtering is used. Two major advantages of DC sputtering for this process are that it is easy to control and is a low-cost option [57]. A schematic of this process is shown in Fig 3.4.

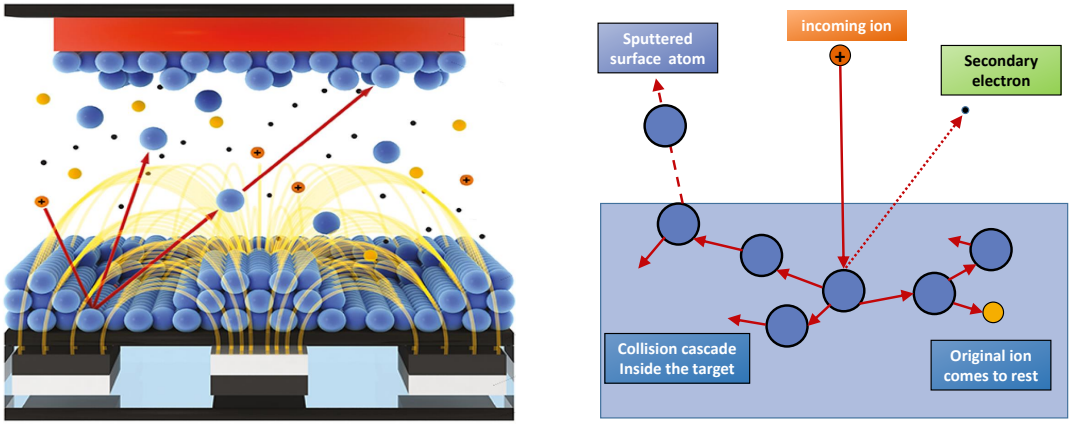

Figure 3.4: Illustration of the sputtering process: The collision cascade in the sputter target is produced by collisions from incident ions. This cascade produces secondary electrons as well as sputtered surface atoms. Fig is adapted from [58]

Problems During the fabrication process, we encountered several problems. The first is the alignment issue during the writing process in the e-beam lithography. In the last few steps of fabrication (top heaters or connection pads), the pattern on the exposed resist can be shifted from its design location, causing misalignment issues and possible device failure. It is caused by the inaccurate positioning of the markers. This well-known problem has now finally been solved by using a different nanobeam alignment routine using the so-called "Overlay"-feature. Details will be discussed in Appendix A.1. Another problem is the quality of the patterned material. First, T_c of the superconductor decreases when fabricated on the YIG substrate. The T_c of niobium patterned on YIG, which is the first chosen superconductor, was around 2K. We then turned to niobium nitride and found a T_c of about 7K to 10K depending on the width and layer thickness of the superconducting layer. Another problem arouse from the top heater structure, which was fragile during experiments and was found to generate large temperature gradients. It might be caused by the bad surface condition of the insulator surface on which the heater is grown.

3.3 Experimental Procedure

In this section, we introduce experimental details of thermopower signal detections. After fabrication, we glue the finalized nanostructure samples on a copper heat sink of a chip carrier and bond connection pads to terminals on the chip carrier using an Al-wired bonder. For measurements, the chips are mounted on a cryostat dipstick and placed in a variable temperature insert (VTI) ($2\,\mathrm{K} \leq T \leq 300\,\mathrm{K}$) of a superconducting magnet liquid helium cryostat, to perform the so-called angle-dependent magnetoresistance (ADMR) measurements. We apply heating currents I_{inj} at one of the heaters and measure the corresponding thermopower signal at different temperatures around T_c in the superconductor when rotating the orientation of the external magnetic field in three orthogonal rotation planes.

Namely, the in-plane (IP), out-of-plane along current (OOPJ), and out-of-plane transverse (OOPT) geometries are shown in Fig 3.5.

Temperature The dipstick heater stabilizes the temperature in the dipstick and the needle valve controls the liquid helium flow. The temperature is measured by the electrical resistance of a resistive temperature sensor. It measures the temperature of the copper heatsink and can be different from the temperature of the superconductor on top of the sample.

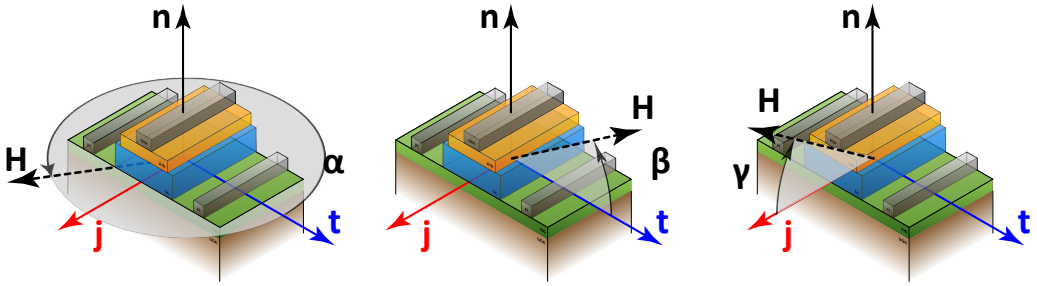

(a) IP rotation plane **(b)** OOPJ rotation plane **(c)** OOPT rotation plane

Figure 3.5: Three rotation geometry using a 3D-vector magnet: (a) IP rotation plane; Rotation angle α is relative to the **t**-axis. (b) OOPJ rotation plane; Rotation angle β is relative to the **t**-axis. (c) OOPT rotation plane; Rotation angle γ is relative to the **j**-axis.

Magnetic Field The magnitude and the orientation of the external magnetic field are controlled by a 3D-vector magnet consisting of three superconducting pairs, which generate orthogonal magnetic fields. The coils can reach a maximum magnetic field strength of up to $\mu_0 H = 2.5\mathrm{T}$ in the horizontal plane and up to $\mu_0 H = 6\mathrm{T}$ in the vertical direction. When we drive charge current in the superconducting coil made of type-II SC to generate the magnetic field, trapped flux arises at the cavities of the SC. The trapped flux can create a pseudo-resistance and depress both critical current density and critical field. For the trapped flux is independent of the applied charge current, it is difficult for the superconducting coil to generate a stable small magnetic field. As the resultant field is generated by three coils, it is less accurate in magnitude during field rotations than rotation measurements in a static magnetic field with a stepper motor.

AC lock-in detection A lock-in amplifier is a type of amplifier that can extract a signal with a known carrier wave from an extremely noisy environment. Depending on the dynamic reserve of the instrument, signals up to a million times smaller than noise components, potentially fairly close by in frequency, can still be reliably detected. It is essentially a homodyne detector followed by a low-pass filter that is often adjustable in cut-off frequency and filter order [59].

The spin injection is transferred into a QP charger signal in the superconductor via the iSHE and can be detected as the voltage on the terminals of the superconductor. There are two main kinds of signals. One is the SHE singal ($V_{\mathrm{SC}}^{\mathrm{el}} \propto I_{\mathrm{inj}}$) introduced in Sec. 2.1 and other one is the SSE signal ($V_{\mathrm{SC}}^{\mathrm{th}} \propto I_{\mathrm{inj}}^2$) defined in Sec. 2.2. To detect the SSE signal and other higher harmonic signals, we use the low-frequency AC lock-in technique in measurements. We apply low-frequency AC charge currents (about 7Hz to 15Hz) to the heater and measure

the frequency-sensitive voltage response at the superconductor. We choose low-frequency 'quasi-DC' currents to decrease the signal from the capacitive/inductive coupling between nanostrips and non-integer frequency (ie. 7.73Hz) to avoid the coupling with the noise from the devices.

In experiments, we apply a sinusoidal AC current $I_{\rm inj} = I_0 \sin \omega t$ with $\omega = 2\pi f$ and I_0 is the amplitude of the injected charge current $I_{\rm inj}$. Correspondingly, the detected voltage signal $V_{\rm det}$ at the superconductor is a function of the driving current $V_{\rm SC} = f(I_{\rm inj})$ with a finite phase delay. Using Taylor's formula, the measured voltage response can be written as

$$V_{\rm SC}(t+\phi) = V_0 + R_1 I_{\rm inj}(t) + R_2 I_{\rm inj}^2(t) + R_3 I_{\rm inj}^3(t) + R_4 I_{\rm inj}^4(t) + o(I_{\rm inj}(t)) \tag{5}$$

where we only focus on the first Four orders and neglect higher-order terms. The coefficients R_n parametrize the conversion processes involved in the magnon transport from the injector to the superconductor. The coefficients R_n can be written as via Taylor expansion

$$R_n = \frac{1}{n!}\frac{d^n}{dI_{\rm inj}^n} V_{\rm det} \tag{6}$$

With the lock-in technology, the $n^{\rm th}$ harmonic voltage signal $V^{n\omega}$ is measured by multiplying $V_{\rm det}(t)$ with two sinusoidal reference signals $\propto \sin n\omega t$ and $\propto \cos n\omega t$ (i.e. shifted by 90°) which are in the same phase with the source current $I_{\rm inj}(t)$. Then, the multiplied signals are integrated over a time interval $T \gg 1/\omega$ via low-pass filtering. In this way, we do a Fourier transform on the function $V_{\rm det} = f(I_{inj})$ and decompose functions into frequency components. Thus, $V^{n\omega}$ is the n^{th} Fourier transformation term of the $V^{n\omega}(t)$ and can be written as

$$\begin{aligned} V_{\rm X}^{n\omega} &= \frac{\sqrt{2}}{T}\int_t^{t+T} \sin(n\omega t') V_{\rm det}(t) dt' \\ V_{\rm Y}^{n\omega} &= \frac{\sqrt{2}}{T}\int_t^{t+T} \cos(n\omega t') V_{\rm det}(t) dt' \end{aligned} \tag{7}$$

denoted by the subscripts X and Y. By plugging Eq.(5) into Eq.(7), the first two harmonic voltage signals can be written as

$$V_{\rm X}^{1\omega} = \frac{1}{\sqrt{2}}(I_0 R_1 + \frac{3}{4} I_0^3 R_3)\cos\phi \quad V_{\rm Y}^{1\omega} = \frac{1}{\sqrt{2}}(I_0 R_1 + \frac{3}{4} I_0^3 R_3)\sin\phi \tag{8}$$

$$V_{\rm X}^{2\omega} = \frac{1}{2\sqrt{2}}(I_0^2 R_2 + I_0^4 R_4)\cos 2\phi \quad V_{\rm Y}^{2\omega} = \frac{1}{2\sqrt{2}}(I_0^2 R_2 + I_0^4 R_4)\sin 2\phi \tag{9}$$

From the above results, the first harmonic signal $V^{1\omega}$ corresponds to effects that are odd under current reversal, which also means that the first harmonic signal is governed by R_1, R_3 and higher odd number coefficients. Similarly, the second harmonic signal $V^{2\omega}$ represents effects that are even under current reversal and is governed by R_2, R_4, and higher even number coefficients. The higher harmonic signals (i.e. third harmonic $V^{3\omega}$ and fourth harmonic $V^{4\omega}$) represent the corresponding higher coefficients in the Eq.(5). Hence, with the help of the lock-in detection, we detect small signals from large noise and distinguish electrically generated signal ($\propto I_{\rm inj}$), thermally generated signal ($\propto I_{\rm inj}^2$) and

even higher order signals ($\propto I_{\mathrm{inj}}^{n}$) in magneto-transport measurements.

The lock-in amplifier exports two series of signals. The finite phase ϕ leads to a distribution of the signal into both the X and Y quadratures of the harmonic voltages. To transfer two quadratures into these contributions into a single quadrature, we apply a rotation matrix to our signals and calculate the rotated quadratures X' and Y',

$$\begin{pmatrix} V_{\mathrm{X}'}^{n\omega} \\ V_{\mathrm{Y}'}^{n\omega} \end{pmatrix} = \begin{pmatrix} \cos n\phi & \sin n\phi \\ -\sin n\phi & \cos n\phi \end{pmatrix} \begin{pmatrix} V_{\mathrm{X}}^{n\omega} \\ V_{\mathrm{Y}}^{n\omega} \end{pmatrix} \tag{10}$$

The phase ϕ is found by applying the rotation matrix to the first harmonic voltages ($n = 1$) and setting the imaginary component in the y-component to zero. Notably, the n^{th} harmonic voltages have to be rotated by $n\phi$ to get the full signal response in either of the two quadratures.

We use two MF2LI $50\,\mathrm{kHz}$ Lock-in Amplifiers from *Zurich Instruments* to record the first, second, third, and fourth harmonic voltage signals at the superconductor and reference detector simultaneously. The voltage signals are pre-amplified by a *SR560* Low Noise Preamplifier. The source injection current is generated by a *Keithley 6221* DC and AC Current Source. The current source and one of the lock-in amplifiers are triggered by the digital output of the other lock-in amplifier to ensure no drifting of the relative phase between the source and reference. When the lock-in amplifiers and source are synchronized, the phase delay between the source current and the measured signal is stabilized.

4 Results

In this chapter, our results for the magnon spin transports of our three-terminal all-electrical thermal spin transport devices are presented. We apply an injection charge current either on the top heater or on the side heater to generate a temperature gradient at the FMI/SC interface and detect the corresponding voltage signals from the NBN strip and reference Pt strip. We first introduce the results on the device without a heater structure patterned on the top of an NbN superconducting strip in Sec. 4.1. Then we introduce the results when using the top heater to generate the temperature gradient on structures with a heater structure on top of the central NbN strip in Sec. 4.2.

4.1 Thermal magnon transports signals with the outer heater

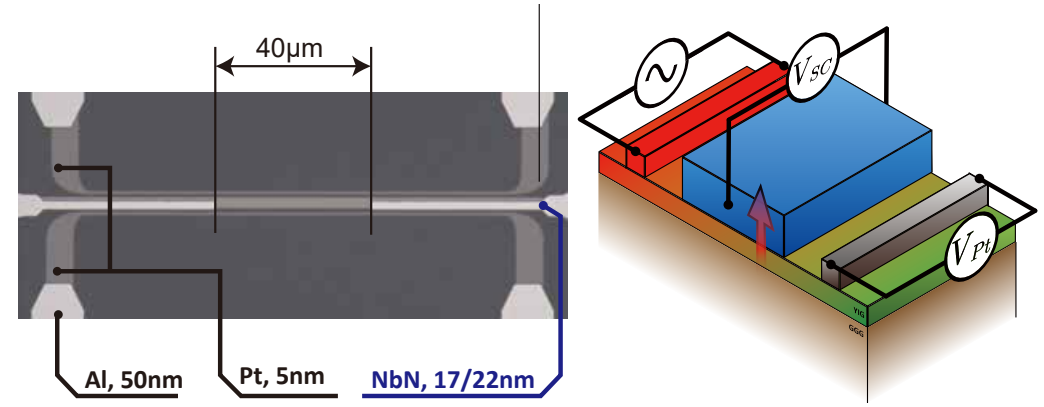

(a) Layout of the structure without a top heater

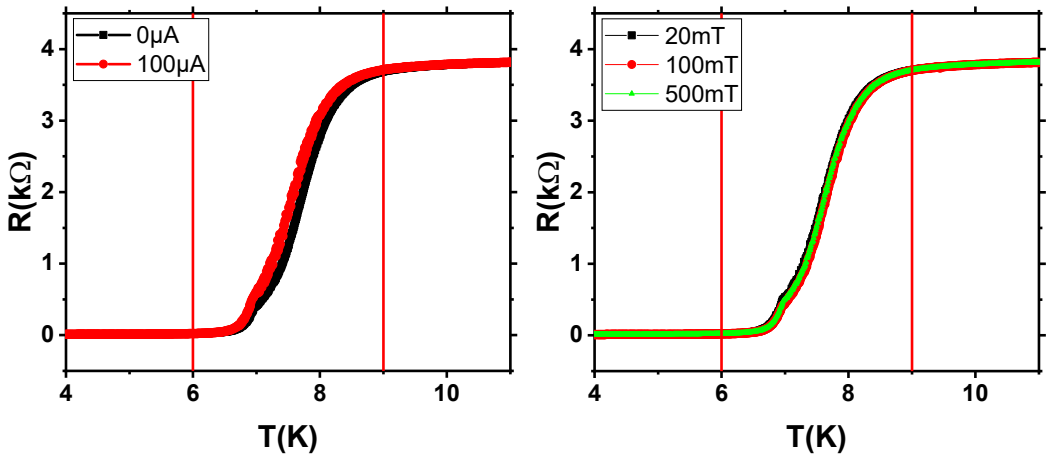

(b) injection current dependence

(c) External field dependence

Figure 4.1: (a) The layout of the structure without a top heater: we pattern two $90\mu m \times 0.5\mu m \times 5nm$ platinum strips as side heaters and detectors, and a $100\mu m \times 2\mu m \times 17nm$ NbN stripe in the middle. We see a small misalignment between the Al electrode and the middle superconducting bar, due to alignment issues during fabrication. (b) The injection current dependence of the resistivity of the NbN strip: the transition temperature is about 7.5K and the injection current has little influence on T_c (c) The influence of the external magnetic field applied along t axis: The external magnetic field has little influence on T_c.

In this section, we present the results of the spin transport signals through the SC/FMI interface when driving heat currents using the outer side heater. We expect to see an en-

hancement of the SSE signal of the superconductor around its critical temperature T_c as reported in Ref. [6]. We first perform our measurements on a simplified structure which have similar geometry to the devices used in Ref. [6]. One advantage of this simplified structure is that it has fewer layers than the structure introduced in Sec. 3.1, which means fewer steps in the fabrication process. Moreover, the results of this structure can work as a good comparison to previous work. But for the lack of a top heater, we can only generate one type of temperature gradient. We observed a rich behavior in the angular dependence of the thermopower signal. Apart from the signal enhancement near T_c, we also observe a shift in the angular dependence, offset, and several sign changes in the transition temperature range.

4.1.1 IP-ADMR measurements

Experimental details We conduct our first measurement on devices without a top heater structure, which is a simplified structure compared to the one introduced in Ch. 3.1. The structure is fabricated on a 2 µm thick LPE-YIG grown on a GGG substrate. we pattern two $90\,\mu\mathrm{m} \times 0.5\,\mu\mathrm{m} \times 5\,\mathrm{nm}$ platinum strips as side heaters and detectors, and a $100\mu\mathrm{m} \times 2\mu\mathrm{m} \times 17\mathrm{nm}$ NbN stripe in the middle. The edge-to-edge distance between the side heaters and central superconductor is 750 nm. The central superconductor is connected to the outer connection pad only with two electrodes. The detailed information on the layout is shown in Fig. 4.1.

Before we conduct the IP-ADMR measurements, we measure the resistance of the central NbN strip to determine the critical temperature T_c. T_c is measured via two-point resistance measurements for different applied AC charge currents (0-200 µA) to the Pt side heater, together with an applied external magnetic field in $\mathbf{t}$ direction, shown in Fig. 4.1b and Fig. 4.1c. The critical temperature is influenced by the external injection currents due to heating(see in Ch. 3.3). Therefore, when we apply an additional temperature gradient by driving a charge current through the outer heater, T_c will decrease with increasing injection currents. The T_c is around 7.5K at zero applied currents and zero applied external magnetic field. We observe a small reduction in T_c for rising injection currents and applied external magnetic fields, but the difference is small ($< 0.1\mathrm{K}$) in our cases. For the following discussion, we define three temperature ranges: the fully superconducting range($T < 6\,\mathrm{K}$), the transition range ($6\,\mathrm{K} < T < 9\,\mathrm{K}$), and the normal state range ($9\,\mathrm{K} < T$).

In the IP-ADMR measurements, we apply 7.737 Hz sinusoidal wave at an applied AC charge current of 100 µA ($I_0 = 100\mu\mathrm{A}, \quad j_{\mathrm{inj}} = 4 \times 10^{10}\mathrm{A} \cdot \mathrm{m}^{-2}$). Also, we apply an external magnetic field $\mu_0 H = 100\mathrm{mT}$, which is rotated in the in-plane direction ($j - t$ plane) by a 3D-vector magnet. At the starting position ($\varphi = 0°$), the applied magnetic field is aligned perpendicular to the Pt strips. We amplify the voltage signals from the NbN strip and Pt strip with a factor of 10000 and filter signals at a high frequency above 100Hz to reduce noise input. Then the voltage signals of the NbN strip and Pt detector are then detected by two separate lock-in amplifiers. We perform a full rotation of the magnetic field from -20° to 380° at steps of 5° for each temperature. The measurement procedure is then repeated for temperatures in the range from 3K to 12K.

Thermal signal with temperature The result of the signals from the 2nd harmonic channel, in which $V^{2\mathrm{nd}} \propto I_{\mathrm{inj}}^2$, is shown in Fig.4.2, the upper panels represent the IP rotation angle α dependence of the second harmonic signal on the superconducting NbN strip ($V_{\mathrm{NbN}}^{\mathrm{th}}$) in three different temperature ranges, while the lower panel is the corresponding second harmonic signal on the Pt strip. From the top panel, we detect no voltage signal in the fully superconducting range($T < 6\mathrm{K}$), while in the normal state range ($9\mathrm{K} < T$), we observe the expected ordinary SSE signals which have cosine angle dependence. In the transition range ($6\mathrm{K} < T < 9\mathrm{K}$), there is an enhanced thermopower signal compared to signals in the normal state range. Moreover, there are two sign changes of the signal at 7.5K and 7.9K.

What stands out in Fig.4.2b is the $V_{\mathrm{SC}}^{\mathrm{th}}(\alpha)$-curve in the transition range ($6\mathrm{K} < T < 9\mathrm{K}$). Compared to the $V_{\mathrm{SC}}^{\mathrm{th}}(\alpha)$-curve in the normal state range, it shows several additional unexpected features. First, there is an unexpected angle offset in angle α (about 60°), which means that the largest signal is not detected when the orientation of the magnetic field is perpendicular to the NbN strip. Furthermore, we observe a large offset in the detected voltage, which only occurs for temperatures in the transition temperature range. Finally, the thermopower signal is enhanced around critical temperature. To further investigate the behavior of the thermopower signal around T_c, we perform a modified cosine function fit on every $V_{\mathrm{SC}}^{\mathrm{th}}(\alpha)$ curve with the form

$$V_{\mathrm{SC}}^{2\mathrm{nd}} = A\cos\lceil\frac{\pi}{180^\circ}(x - x_c)\rceil + y_0 \tag{11}$$

with three parameters: Amplitude A, phase shift ϕ and offset y_0. The range of three parameters is $0 < A, \quad 0^\circ < \phi < 360^\circ$. Fig.4.3 shows the temperature dependence of the three fitting parameters.

Amplitude, offset and phase shift We focus on the temperature dependence of the amplitude first. The amplitude of the thermal signal exhibits three peaks in the temperature dependence curve. The biggest peak is observed at 7.7 K, which approximately matches the T_c of the NbN strip, with a magnitude of 200 nV. This may indicate that the SSE signals in the NbN are enhanced at the temperature near T_c. This behavior is compatible with recent theoretical predictions [14, 60] and experimental reports on FMI/SC structures [6, 61, 62]. There it has been found, that while (spin-triplet) Cooper pairs from the SC cannot leak into the FMI even if the exchange spin-splitting can still penetrate the SC [63]. The superconducting quasiparticles at the FMI/SC interface [40] are available for spin current transport and give rise to a distinct coherence peak around T_c due to the large QP density of states (DOS). This gives rise to an enhancement of spin absorption by the adjacent SC near T_c. The multiple structures originate from the sign change of the SSE signal. The sign changes of the SSE signal will be discussed in detail in this section later.

Next, we focus on the unexpected phase shift in angle dependence of the SSE signals in the transition range. As there is no signal in the fully superconducting temperature range, we are not able to reliably quantify the signal phase and hence set it to be equal to the one in the normal state range. When raising the temperature from the fully superconducting range to the transition, the phase shift occurs as the thermopower signals appear. Also because of the sign change of the signals, there are two rapid 180° changes correspondingly.

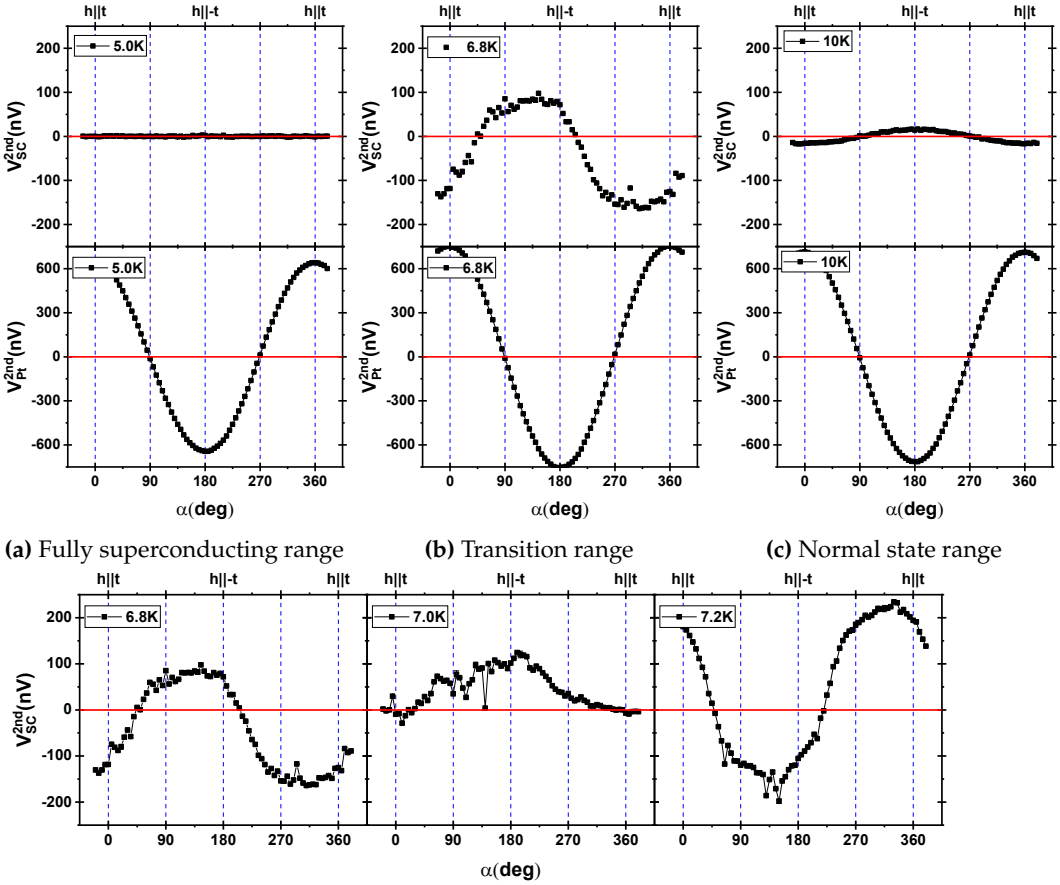

(a) Fully superconducting range **(b)** Transition range **(c)** Normal state range

(d) Detailed results in the transition range

Figure 4.2: Angular dependence of the SSE signals in NbN (upper panel) and Pt strips (lower panel). (a) The fully superconducting range: We detect no signals in the fully superconducting range (b) The transition temperature range: We detect the signals with unexpected phase shift and offset. (c) The normal state range. (d) Detailed results in the transition range: The behaviors of the SSE signals exhibit several sign changes in the transition temperature range.

As in the fitting function, we restricted the amplitude A to a positive value, the sign changes will give rise to a 180° change in the phase parameter. Then the phase shift gradually reduces with the temperature increasing from the transition range to the normal state range. The manifestation of the phase shift in the transition range shows that there are some other mechanisms at play in addition to the SSE signal. One of the possible factors contributing to the phase shift is the influence of the small OOP component of the external magnetic field. Because of the sample mounting on the chip carrier, we can also not rule out a small OOP component of our sample plane with respect to the external field. It seems that the small out-of-plane component contributes to the angle-dependent thermopower signal via the formation of superconducting vortices. This will be discussed in greater detail in later parts of this thesis.

Finally, we discuss the offset of the thermopower signals. As is shown in Fig.4.3c, the offset in the voltage signals occurs only in the transition temperature range and vanishes in the normal state range. Surprisingly, the offset changes its sign three times in the transition temperature range. Compared to the value of the amplitude, the offset is of a comparable magnitude for certain temperatures. There are several mechanisms that contribute to

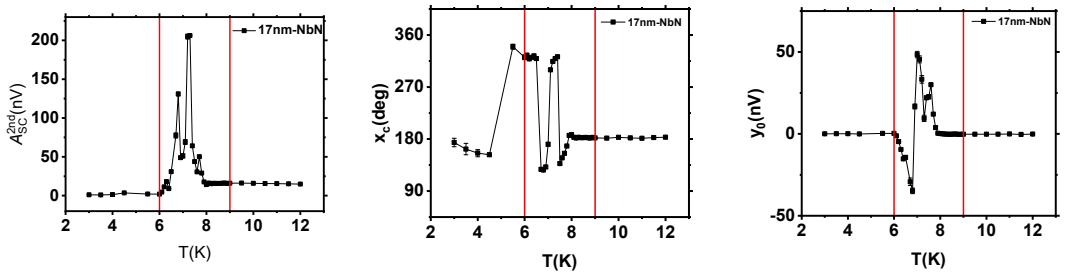

(a) Amplitude $A(T)$ **(b)** Angle offset $x_c(T)$ **(c)** Offset $y_0(T)$

Figure 4.3: Temperature dependence of the fitting parameter. (a) Temperature dependence of the amplitude; We detect no signals in the fully superconducting range, enhanced signals in the transition temperature range, and weak signals in the normal state range. (b) Temperature dependence of the shift in angle position; We observe a shift in angle position of about 60° in the transition temperature range. (c) The temperature of the offset; We detect a large offset only in the transition temperature range

this large offset. On the one hand, the capacitive/inductive coupling of the AC current between the Pt strip and the NbN strip might yield additional contributions. However, the frequency is quite low in our experiment and thus should not lead to a detectable coupling effect. Also, this phenomenon cannot explain why such a large coupling effect should manifest only in the transition temperature range. The other factor is the influence of the OOP magnetic field component and associated vortex effects might contribute as mentioned above.

Conclusion The rich behaviors of the thermopower signals indicate that there are several additional mechanisms contributing to the spin transport process at the FMI/SC interface. There exist several potential origins of the rich behaviors of the thermopower signals. First, these behaviors could originate from the magnon accumulation in the YIG layer. Since the associated SSE signal can not the deviation from a $\cos\alpha$ dependence on the orientation of the magnetic field of the detected voltage signals, the spin polarization of the magnons in the thick YIG layer (up to 2 μm) exhibits some unexpected properties. Next, the behaviors of other spin carriers in the SC contribute to these unexpected phenomena. Not only spin-triplet Cooper pairs at the SC/FMI interface but also the QPs and the vortices can carry spin. Spin-triplet Cooper pairs, QPs, and vortices might have different charge-spin balances and interact with each other to give rise to the rich behaviors in thermopower signals. Finally, there might also exist other spin currents in the SC driven by the temperature gradient in the SC, and affect the signals we detect. To further study the origin of unexpected phase shifts and large offset signals, we performed more experiments in different geometries to identify the dependence of the offset and the phase shift on temperature and rotation plane.

4.1.2 Out-of-plane rotation planes ADMR measurements

As mentioned in the previous section, a rich behavior in the ADMR is observed in our sample in the transition temperature range. The OOP component of the magnetic field may play an important role in the process, so we conduct other transport experiments when the

orientation of the magnetic field is rotated in other rotation planes.

Experimental setup We perform our measurements on the same structure as the results shown in the previous section. The experimental setup is the same as for the IP-ADMR measurements but we rotate the magnetic field in the OOPJ and OOPT rotation planes (see in Ch.3.3). We apply 7.737Hz sinusoidal wave at an applied AC charge current of 100µA ($I_0 = 100\mu\mathrm{A}, \quad j_{inj} = 4 \times 10^{10}\mathrm{A} \cdot \mathrm{m}^{-2}$). Also, we apply an external magnetic field $\mu_0 H = 100\mathrm{mT}$, which is rotated in the OOPJ geometry ($n - t$ plane) and OOPT geometry ($n - j$ plane) by a 3D-vector magnet. At the starting position ($\varphi = 0°$), the applied magnetic field is aligned perpendicular to the n-axis.

Results Fig. 4.4a shows the second harmonic signals on the NbN and Pt strips in the OOPJ rotation plane, while Fig. 4.4b shows the signals in OOPT geometry. Similar to the IP results, we detect weak signals in the fully superconducting range, signals with rich angular dependence in the transition range, and the expected ordinary signals in the normal state range. The angle dependence of OOPJ and OOPT signals for the NbN is similar to each other, while the results on the Pt are compatible with recent reports [12, 26]. It is surprising to see that the thermopower signal on the NbN strip undergoes a sign-change at the position $\beta(\gamma) = 180°$ where the magnetic field is aligned in the in-plane direction. It shows that when the normal component of the magnetic changes its sign, the signal changes its sign correspondingly, which indicates that the contribution of the OOP component takes priority to the thermopower signal.

Conclusion The rapid signal change when $\beta(\gamma) = 180°$ shows that even a small OOP component of the magnetic field can significantly influence the results of the IP-ADMR measurements. There are two main effects that might contribute to it. One is the superconducting Nernst effect [64, 65] and the other is the spin vortex in the type-II superconductor [66]. The vortices can also be spin-polarized and generate spin current J_s and might have different spin-charge conservation relations with the external magnetic field. But as the signals originating from the OOP component of the external magnetic field are dependent on the direction with respect to the **n**-axis, they correspondingly exist some angular dependence in which we will get some positive signals when the OOP component of the magnetic field is positive and the negative signals when the OOP component is negative. Therefore, we infer, that the signals, originating from the OOP component of the external magnetic field in IP geometry, do not contribute to the offset (angular independent signals) in IP ADMR results.

4.1.3 Electrical current and magnetic field dependence

To further investigate the thermopower signals in the transition temperature range, we vary several experimentally accessible parameters. In detail, three parameters: the injection current I_{inj}, the intensity of the external magnetic field $\mu_0 H$, and the thickness of the superconducting NbN strip, are varied in this section.

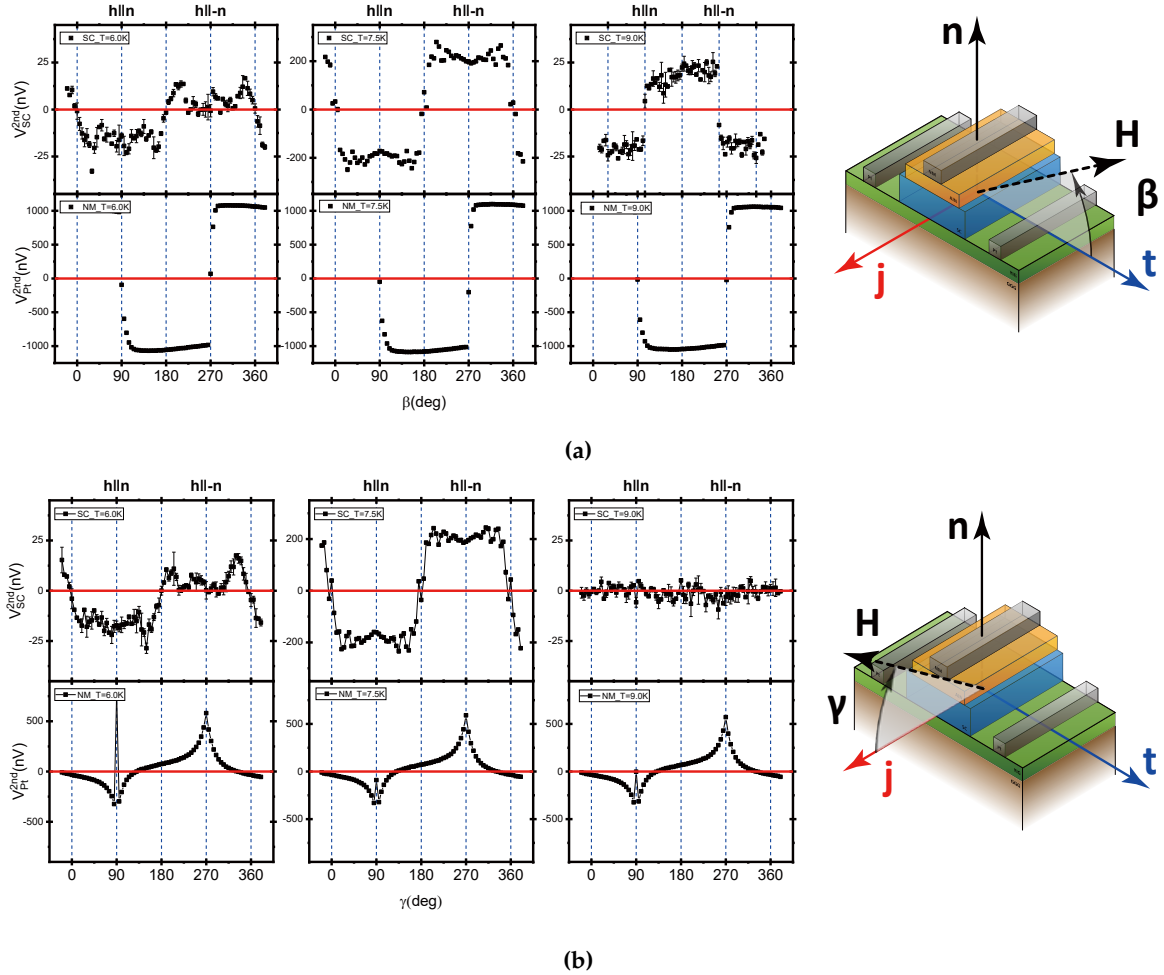

Figure 4.4: OOPJ and OOPT Pt and NbN ADMR results: (a) The OOPJ NbN and Pt results. The upper panels show the NbN results while the lower panel shows the Pt results at the fully superconducting range (6K), transition range (7.5K), and normal state range (9.0K). (b) The OOPT results. It illustrates that the SSE signals exhibit a rapid sign when the normal component of the magnetic field changes its sign

Current dependence The AC injector current dependence on the signals will be discussed in this section. The only parameter we change compared to the experiments in Sec. 4.1.1 is the injection current I_{inj}. We compare the results of an injection current of 100 µA and 200 µA results in this section. As is mentioned in Sec. 4.1.1, the value of the injection current will influence T_c measured in our devices. The difference of T_c between 100 µA and 200 µA are shown in Fig. 4.1, which illustrates there are no great differences.

From the IP-ADMR experiments, we extract the amplitude A, angle shift x_c, and offset y_0 by fitting Eq. 11 to obtain the data. As is shown in Fig. 4.5, the temperature dependence of $I_{\text{inj}} = 100\mu\text{A}$ (black line) and $I_{\text{inj}} = 200\mu\text{A}$ (blue line) is the same. In the $A(T)$ curve, we can see that the peak shifts with the T_c but the peak magnitude is comparable. Focusing on the normal state range, the amplitude for 200 µA is 4 times that for 100 µA, which is compatible with the assumption $V^{2nd} \propto I_{\text{inj}}^2$. The phase shift remains the same, which shows that the strength of the heating currents does not affect it. However, the offset increases drastically with rising injector currents. As the offset is not a linear function of I_{inj}, we infer that it does not originate from the capacitive/inductive coupling between the NbN and Pt strips.

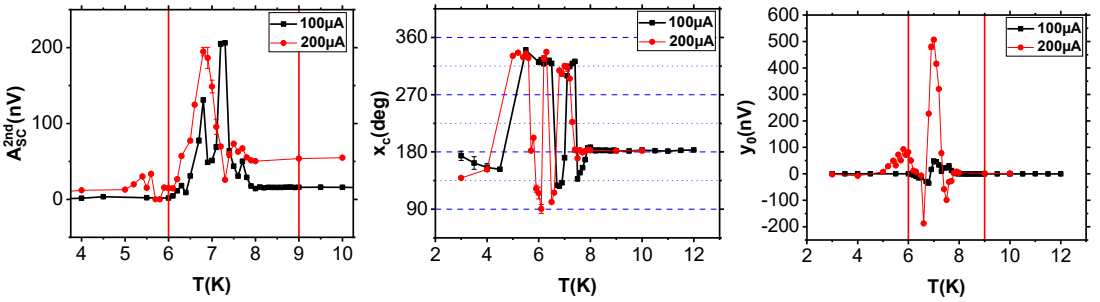

(a) Amplitude $A(T)$ **(b)** Angle offset $x_c(T)$ **(c)** Offset $y_0(T)$

Figure 4.5: Current dependence of fitting parameters in IP-ADMR measurements using different injection currents (100µA and 200µA) (a) amplitude $A(T)$: The amplitude increases with the increasing injection charge currents at the temperatures in the normal state (b) Angle offset $x_c(T)$: The shift in angle position remains same using 100 µA and 200 µA. (c) offset $y_0(T)$: The offset is greatly enhanced by the applied charge currents

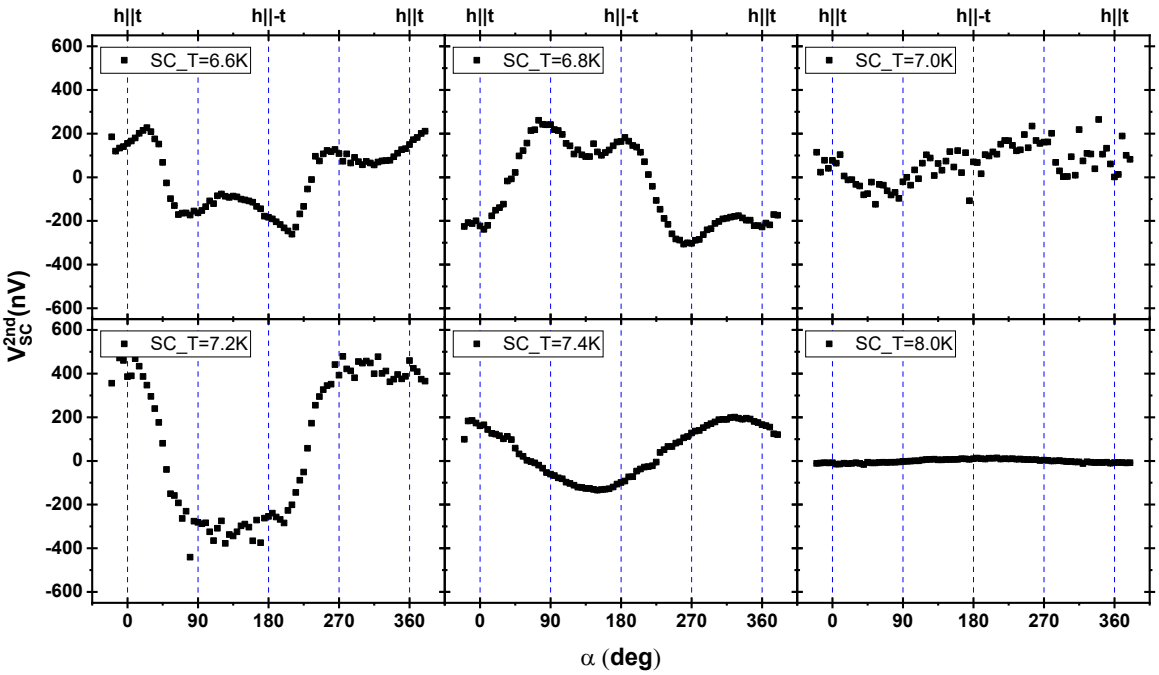

Figure 4.6: The angular dependence of the SSE signals when a 500mT external magnetic field is rotated in-plane in the transition temperature range (6.6K-8.0K). The results at the temperatures 6.6K and 6.8K, the angular dependence is out of cosine shape. With the temperature increases, the dependence is transferred into a cosine shape at temperatures 7.2K and 7.4K.

Magnetic field dependence We focus on the behavior of the SSE signals for different magnetic field magnitudes. The magnetic field is again rotated in the $\mathbf{j} - \mathbf{t}$ plane but for different magnitudes of the applied external field. We compare the $V_{\mathrm{SC}}^{\mathrm{th}}(\alpha)$ dependence for magnetic field magnitudes of 100mT and 500mT. we first focus on the 500mT results. With the increase of the magnetic field, the dependence strongly deviates from the cosine shape at the beginning of the transition temperature range (see 6.6 K, 6.8 K in Fig. 4.6). The signature is indicative of the presence of additional periodic signals with a different periodicity. Comparing these ADMR results to the OOP results in Fig. 4.4, we can assume that the OOP component of the external magnetic field gives rise to an additional signal with a different period. The signals with other periods decrease with the increasing temperature and it is

sensitive to the magnitude of the external magnetic field. The signals with other periods will be discussed later in Ch. 4.2.4.

NbN thickness dependence We here present the thickness dependence of the thermopower signals, comparing the results on 17nm and 22nm NbN strips. The two devices are fabricated on different chips, but the geometry of the devices remains the same. The two experiments are performed under the same conditions with the amplitude of the injection currents $I_{\mathrm{inj}} = 100\mu\mathrm{A}$ and $\mu_0 H = 100\mathrm{mT}$ magnetic field in-plane. The comparison of the amplitude, phase shift, and offset are shown in Fig. 4.7. We see, that the amplitude of thermopower signals is enhanced with the decrease in the thickness of the NbN strips. This is in agreement with expectations from literature[6]. The offset of the 22nm device is also larger than it of the 17nm device, with similar behaviors. The phase shifts change from 45° on the 17 nm strip to 60 ° on the 22nm strip. It illustrates that the thickness of the strip can influence the phase shift, but because the two devices are fabricated on different chips at different times and mounted on different carriers, the difference might originate from a variation in sample mounting and trapped flux from the magnet.

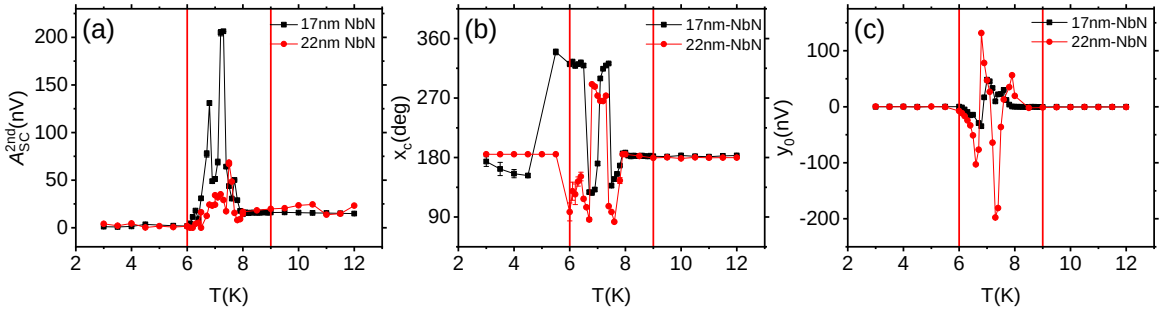

Figure 4.7: The IP-ADMR results comparisons of 17nm and 22nm NbN strip devices. The results is measured with $I_{\mathrm{inj}} = 100\mu\mathrm{A}$ using the side heater and $\mu_0 H = 100\mathrm{mT}$ rotated in-plane. The red data points represent the result of the 22nm thick NbN strip and the black ones that of the 17 nm thick sample. (a) $A(T)$ Amplitude comparison; (b) $x_c(T)$ angle shift comparison; (c) $y_0(T)$ Offset comparison.

4.1.4 Comparison of AC and DC measurement methods

DC detection Results in IP orientation The results reported in Jeon's work [6] exhibited no angle shift and no offset. They used the DC detection method to detect the voltage signals, while we use AC lock-in detection. To figure out whether the unexpected shift in angle position and offset originate from the AC detection technique, we perform a DC measurement on the same structure. We apply a 200 µA DC charge current on the outer heater instead of AC currents. The external magnetic field is rotated in the IP-geometry with the same magnitude $\mu_0 H = 100\mathrm{mT}$.

To distinguish the electrical signals ($\propto I_{\mathrm{inj}}$) and the thermal signals ($\propto I^2_{\mathrm{inj}}$), DC currents of positive($+I_{\mathrm{inj}}$) and negative (I_{inj}) polarity are applied subsequently to the Pt strip. the corresponding V^+ and V^- at the NbN strip and the reference Pt strip are recorded accordingly. As the electrical voltage contributions V^+ switch sign under polarity change (i.e. $V^{\mathrm{el}}_{\mathrm{SC}}$ is proportional to odd powers of I_{inj}) and thermal voltages are even under current reversal (i.e. $V^{\mathrm{th}}_{\mathrm{SC}}$ is proportional to even powers of I_{inj}), we can calculate the contributions as

$$V_{\mathrm{SC}}^{\mathrm{el}} = \frac{1}{2}(V^+ - V^-) \qquad V_{\mathrm{SC}}^{\mathrm{th}} = \frac{1}{2}(V^+ + V^-) \tag{12}$$

For the usual DC transport measurements, we use a *Keithley 2400 Sourcemeter* to drive a charge current through the outer heater and measure the respective voltages at both the NbN strip and the reference Pt strip with two *Keithley 2182* nanovoltmeters. To decrease the noise, we repeat the current reversal 5 times for each external direction parameter setting. We perform the same modified cosine function fitting as in the Sec.4.1.1 to the angle dependence of the voltage signals $V_{\mathrm{SC}}^{\mathrm{th}}$.

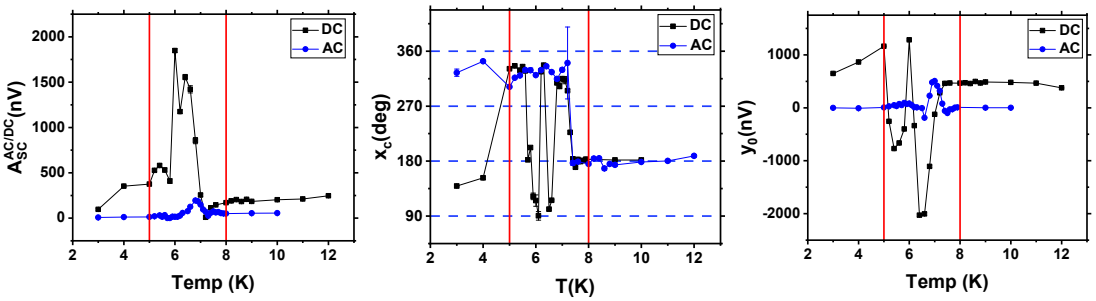

(a) Amplitude $A(T)$ **(b)** Angle shift $x_c(T)$ **(c)** Offset $y_0(T)$

Figure 4.8: Comparison of the results between using DC current (black) and AC current (blue) based detection scheme. For the lock-in detection, we apply a 7.737Hz sinusoidal wave with an amplitude of 200µA through the injection Pt strip. For the DC detection, we apply a 200µA DC charge currents through the injection Pt strip. We compare three fitting parameters. (a) amplitude $A(T)$: The amplitude is significantly larger when using DC currents than when using AC currents, due to the double heating power. (b) agnle shift $x_c(T)$: The shift in angle position remains the same using AC currents and DC currents. (c) offset $y_0(T)$: The observed offset is significantly larger for applied DC currents than in the AC-case.

Fig. 4.8a shows the results of the temperature dependence of the amplitude in the DC set-up. Compared to the signals of the AC set-up (black squares), we get a significantly large magnitude of amplitude with similar three peaks. The large thermopower signals in the DC set-up originate from the increased heating power of the DC current. However, when we focus on the phase shift, the phase shift remains the same (60°). The temperature dependence of the offset also shows no differences between the AC set-up and the DC set-up. So we conclude, that the phase and large offset do not originate from the AC-current-based lock-in detection technique. We infer, that the AC lock-in detection technique is reliable in our experiments. Moreover, the capacitive/inductive coupling from the AC currents does not contribute to behaviors of phase shifts and large offsets.

4.2 Thermal magnon transport experiments with top heater structure

In the last chapter, we have presented the results of thermal signals on the devices without a top heater structure. In this section, we will show the results on devices with a top heater (see in Sec. 3.1) to investigate the influence of different temperature gradients.

4.2.1 Results of 2^{nd} harmonic signals

Experimental set-up The detailed layout of the devices is presented in Fig. 4.9. The devices are fabricated on a 2 µm thick LPE-YIG on a GGG substrate, consisting of two $80\,\mu\text{m}\times 0.5\,\mu\text{m}\times 5\,\text{nm}$ platinum strips as side heater a reference detector and a $100\,\mu\text{m}\times 6\,\mu\text{m}\times 17\,\text{nm}$ superconducting NbN stripe in the middle with a 4 µm wide and 35 nm thick AlN insulation layer on top. Furthermore , we fabricate a $100\,\mu\text{m}\times 0.5\,\mu\text{m}\times 15\,\text{nm}$ Pt strip on top working as a top heater. The superconducting NbN strip is connected to the outer pad with four Al electrodes patterned on top.

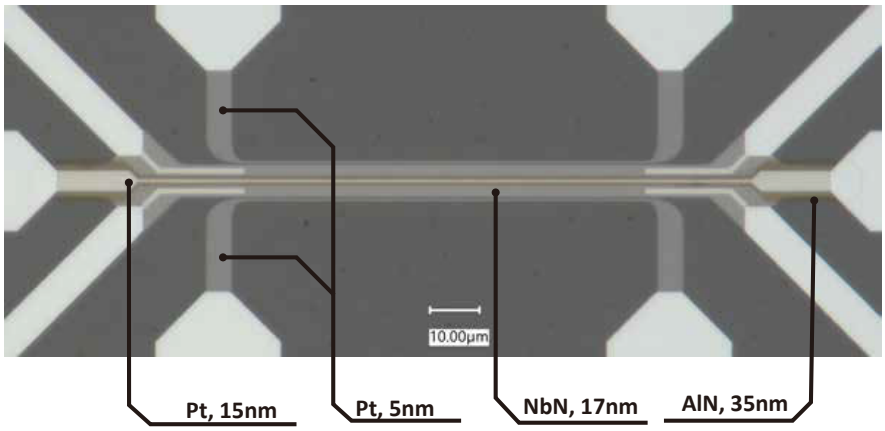

(a) Structure with a top heater

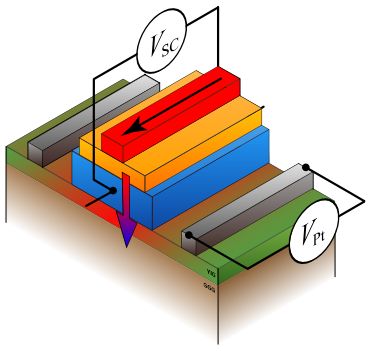

(b) Experimental setup using top heater

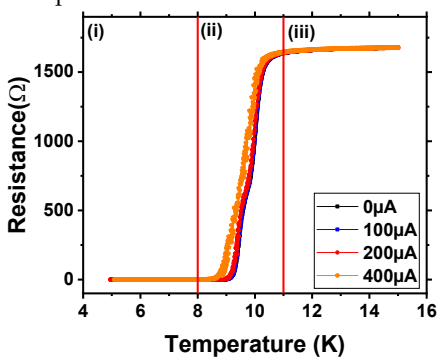

(c) Normal state range

Figure 4.9: (a) Picture of a fabricated structure with a top heater; (b) The experimental setup when using the top heater: we drive a charge current on the top heater and measure the corresponding voltage signal at the superconductor; (c) T_c measurements with different injection currents and no external magnetic field: We measure T_c when driving charge current on the top heater with amplitudes of 0µA, 100µA, 200µA, and 400µA without external magnetic field. We define three temperature ranges: (i) Fully superconducting range ($T < 8\text{K}$); (ii) Transition temperature range ($8\text{K} < T < 11\text{K}$); (iii) Normal state range ($11\text{K} < T$).

We first perform the IP-ADMR measurements using the top heater. The thickness of the

center NbN strip is again set to 17 nm for a better comparison to the results of the previous section. We drive a 7.737 Hz sinusoidal charge current with an amplitude of 200 µA through the top heater and apply an external magnetic field rotated in the $\mathbf{j} - \mathbf{t}$ plane. We detect the voltage signals from the superconducting NbN strip and reference Pt strip by two separate lock-in amplifiers. The signals are amplified by a pre-amplifier with a factor of 10000 and filtered with a low pass above 100Hz just like for the experiments in the previous section. At the start position $\alpha = 0°$, the magnetic field is aligned perpendicular to the NbN strip.

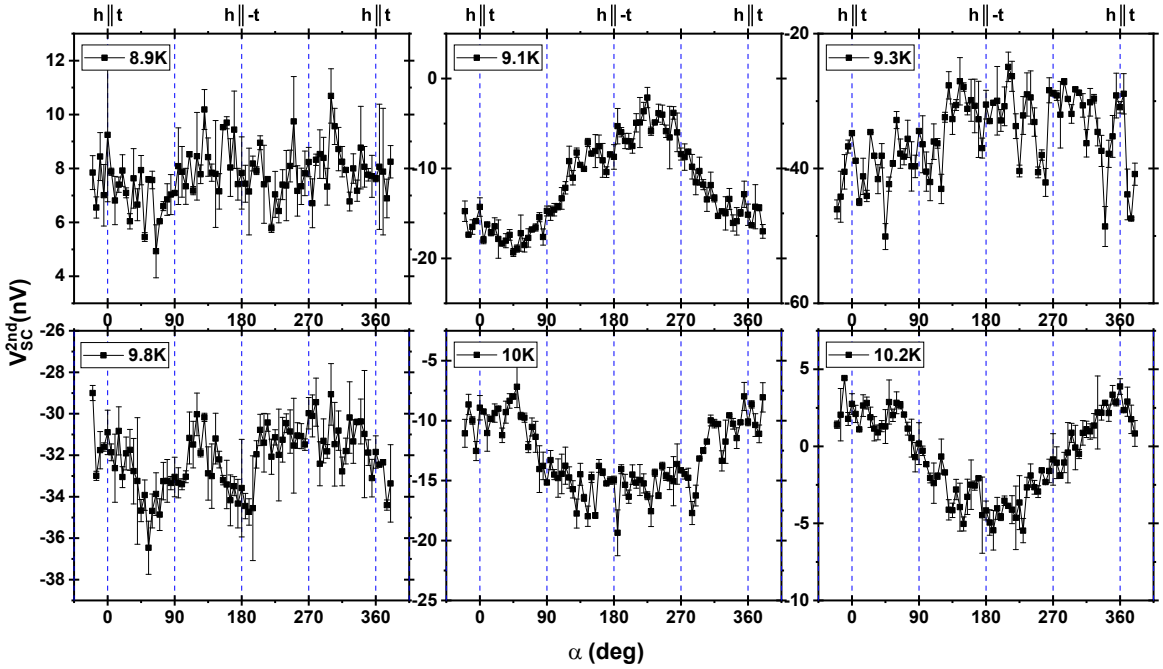

(a) Transition temperature range

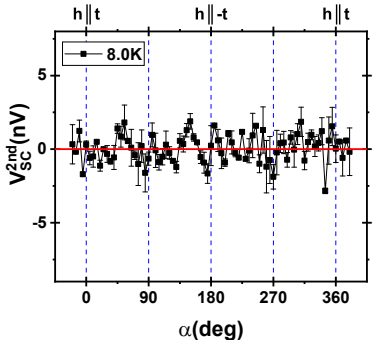

(b) Fully superconducting range

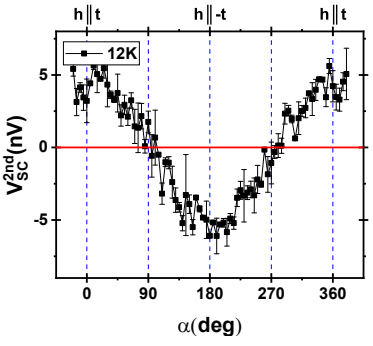

(c) Normal state range

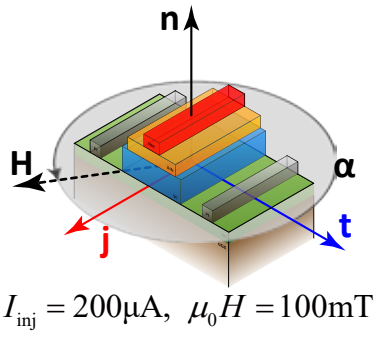

(d) Experimental set-up

Figure 4.10: The angular dependence of second harmonic signals from the NbN strip $V_{\mathrm{SC}}^{2\mathrm{nd}}(\alpha)$ (a) $V_{\mathrm{SC}}^{2\mathrm{nd}}(\alpha)$ in the transition temperature range. There exhibits the offset, phase shift, and sign change same as the IP-result with side heater 4.1.1. (b) $V_{\mathrm{SC}}^{2\mathrm{nd}}(\alpha)$ in the fully superconducting range. No signals are detected. (c) $V_{\mathrm{SC}}^{2\mathrm{nd}}(\alpha)$ in the normal state range. We detect the expected ordinary SSE signal. (d) Schematic illustration of the sample geometry.

Results and current dependence Fig. 4.10a shows the IP-ADMR results for six temperatures (8.9 K, 9.1 K, 9.2 K,9.8 K, 10 K, and 10.2 K) in the transition temperature range from the superconducting NbN strip. As is shown in Fig. 4.10b, we detect no signal in the fully superconducting range. Compared to the results in Sec. 4.1.1, in which we use the side

heater, the angular dependence of the 2nd harmonic signals from the NbN strip $V_{\mathrm{SC}}^{2\mathrm{nd}}(\alpha)$ behaves similarly. The second harmonic signal is enhanced around T_c, and exhibits large offset and shift in angle position only in the transition temperature range.

We perform the same modified cosine function fitting in Sec. 4.1.1, using Eq. 11. The fitting results of amplitude A, agnle offset x_c, and offset y_0 shown in Fig. 4.11. It exhibits richer behaviors than the results in Sec. 4.1.1. First, the temperature dependence of the amplitude $A(T)$ exhibits two peaks at 9 K and 10 K in the transition temperature range, which seems to indicate there exhibit two critical temperatures T_c of the NbN strip. It might originate from the decreased T_c of the patterned fraction of the NbN strip, that is covered with the insulation AlN layer, mentioned in Sec. 3.2. Focusing on the shift in angle position, the shift is about 40° at 9K around the first peak and 20° around the second peak. The opposite direction of the temperature gradient across the FMI/SC interface does not affect the phase shift in experiments. In addition, the behaviors of the temperature dependence of the offset remain the same as the results for the side heater (Sec. 4.1.1).

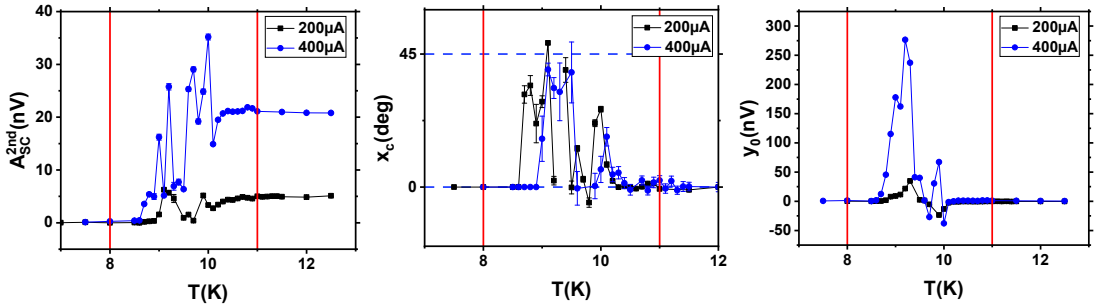

(a) Amplitude $A(T)$ **(b)** Angle shift $x_c(T)$ **(c)** Offset $y_0(T)$

Figure 4.11: Temperature dependence of fitting parameters on the NbN strip using different injection currents. (a)Temperature dependence of the amplitude $A_{\mathrm{SC}}^{2\mathrm{nd}}(T)$ when applying 200μA and 400μA charge currents; (b)Temperature dependence of the angle shift $x_c(T)$; The shift in angle position is around 30°. (c)Temperature dependence of the offset $y_0(T)$

As a next step, we focus on the current dependence of the fitting parameters. As is shown in Fig. 4.11, we compare the results of IP-ADMR measurements using a 200 μA and 400 μA injection currents on the top heater with a magnitude of the external magnetic field $\mu_0 H = 100\mathrm{mT}$. The amplitude is enhanced due to the increasing injection currents, which is comparable to the behaviors of the fitting parameters for the structure using the side heater in Fig.4.5a. The phase in angle position also remains largely the same within the error bars of the fitting process using different injection currents. The phase shift is hence not a thermal-related phenomenon. The offset is enhanced significantly with increasing applied charge current.

4.2.2 Results for 1st and 3rd harmonic signals

In this section, we present the results of the 1st and 3rd harmonic signals. For the 1st harmonic signals, which correspond to effects that are odd under current reversal (see in Sec. 3.3), we only expect weak signals due to the low temperature we perform our experiments at [12, 35]. However, we detect temperature dependence signals in the 1st and 3rd harmonic signals, which do not depend on the orientation of the external magnetic field,

shown in Fig. 4.12.

Experimental set-up Fig. 4.12 shows the temperature dependence of the 1^{st} and 3^{rd} harmonic signals when we apply 200µA and 400µA charge currents on the top heater. We record the results simultaneously with the results shown in the previous section. As the signals exhibit a weak angular dependence, we set the magnitude of 1^{st} and 3^{rd} signals as the mean value over the full angle range at each temperature point.

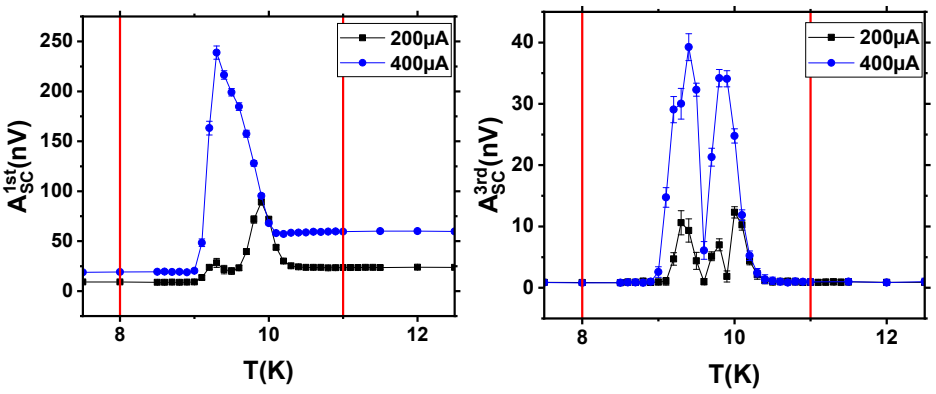

(a) 1^{st} harmonic signal **(b)** 3^{rd} harmonic signal

Figure 4.12: The temperature dependence of the mean value of (a) the 1^{st} harmonic signal $A_{\text{SC}}^{\text{1st}}$ and (b) the 3^{rd} harmonic signal $A_{\text{SC}}^{\text{3rd}}$, when applying 200µA(black) and 400µA(blue). The 100mT magnetic field is rotated in-plane. Both the 1^{st} and the 3^{rd} harmonic signal are enhanced in the transition temperature range.

Result Interestingly, we detect unexpected large 1^{st} and 3^{rd} harmonic signals in the transition temperature range. Focusing first on the 1^{st} harmonic signals, we detect a weak signal in the fully superconducting and a strong signal in the normal state range. Moreover, in the transition range, the signals are enhanced and exhibit two peaks of a similar magnitude to the ones of the 2^{nd} harmonic signals in Sec.4.2.1. Because the signals in the normal state range exhibit a linear response with the magnitude of the charge currents, signals in the 1^{st} harmonic signals might originate from the capacitive/inductive coupling or a potential leackage current between the top heater and the NbN strip. Regarding the 3^{rd} harmonic signals, we detect no signals in the fully superconducting range and the normal state range, while we detect the enhanced signals in the transition range. The behaviors in the transition range also exhibit two peaks. The 1^{st} and the 3^{rd} harmonic signals both increase with the increasing injection currents in the transition temperature range. The mechanism that contributes to the enhancement of the signals in the transition temperature range is still unknown to us and needs further investigation.

4.2.3 Results for magnetoresistance of NbN in the transition temperature range

To further investigate the origin of the shift in angle position and offset, we here present the results of the angular dependence of the resistivity in the transition temperature range.

Experimental set-up We drive a 10µA DC charge current through the NbN strip with two of the four electrodes contacting the NbN and measure the corresponding voltage signal

with the other two electrodes, a 4 point resistance measurement. Meanwhile, we rotate the external magnetic field with a magnitude of 100, in different rotation planes. In this experimet, we do not drive any charge currents through either the top heater or the side heater. Only a weak temperature gradient may manifest in the transition range of SC, due to the charge current flowing through the NbN layer.

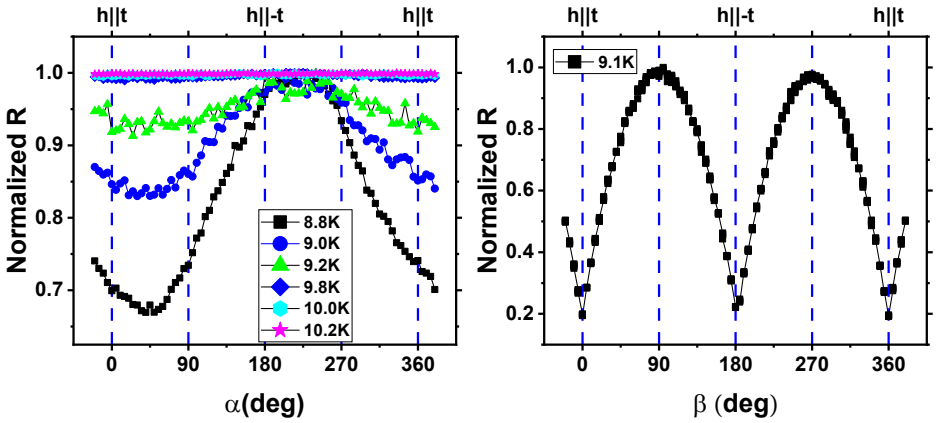

(a) Results of in-plane rotation **(b)** Results of OOPJ rotation

Figure 4.13: The results of normalized resistance when the external magnetic field is rotated in $j-n$ plane (IP) and $t-n$ plane (OOPJ). The voltage is detected when driving a 10µA DC charge current through the NbN strip. The magnitude of the external magnetic field is 100mT. (a) Normalized results when the magnetic field is rotated in IP geometry. The angular dependence of the resistance is in a cosine shape with a 45° angle offset. The amplitude of the resistance decrease with increasing temperature. (b) Normalized results when the magnetic field is rotated in OOPJ geometry.

Results We introduce results when the external magnetic field rotates in-plane at the temperature in the transition temperature range. Fig. 4.13a shows the results of the angular dependence of the resistance. The resistance in different temperatures is normalized by its maximum values. The most interesting part of the results is that the normalized $R(\alpha)$ show a cosine shape with its mininum at $\alpha = 45°$. The amplitude of the resistance decrease with increasing temperature, and the shift remains the same when the temperature rises. Then, Fig. 4.13b shows the results at 9.1K when the external magnetic field rotates in OOPJ geometry. The result is in a $|\sin(\beta)|$-shape. The behaviors of the resistance when magnetic rotates in OOPJ geometry originate from the OOP component of the magnetic field.

Conclusion As the external magnetic field can break the cooper pairs in the superconducting NbN strip, the resistivity increases with the increasing magnitude of the OOP component. Therefore, the minimum resistance is detected when the orientation of the magnetic is either parallel or anti-parallel to the t axis. But the influence of the OOP component of the external magnetic field cannot explain the results when the magnetic field rotates in-plane. The resistance change of SC is independent of the direction of the OOP component of the magnetic field. The $R(\alpha)$-curve should be in the shape of $|\sin(\alpha)|$ but not a cosine shape. Therefore, we infer, that the behaviors of the in-plane results do not originate from the small OOP component from the mount of samples. A mechanism related to the in-plane magnetic field contributes to the resistance change. The phase shift of

the resistivity is comparable to the phase shift in the 2nd harmonic signals so the resistance change might contribute to the agnle shift of SSE signals. One is the additional spin current originating from the charge current in the SC. One similar case is the spin Hall magnetoresistance observed in the Pt strip [67]. But the spin Hall magnetoresistance shows a $\sin^2(\alpha)$ shape in angular dependence and it is proportional to the I_{inj}, which will not contribute to the signals in the 2nd harmonic channel. Another potential is the spin Nernst effect [68]. Also, the SNE shows a similar angular dependence $\sin^2(\alpha)$. The other one is the spin current carried by the vortices in the superconductor. The small OOP component excites the vortices in the type-II superconductor and the movement of the vortices in the presence of the external magnetic field gives rise to the resistance change. But how this mechanism influences and where it originates from still requires further investigation.

4.2.4 Results for a three-terminal spin transport device with a 12nm NbN strip

Experimental setup We perform an IP-AMDR measurement on the structure with a 12nm NbN strip. The layout of the structure is the same as the experiments in the previous section (Sec. 4.2.1). Also, the experimental setup is the same. We drive a 100µA charge current through the top heater with an AC source and detect the corresponding voltage signal from the superconducting NbN strip with a lock-in amplifier when rotating a 100mT external magnetic field in IP geometry. The T_c of the 12nm thick NbN strip is around 7.5 K as shown in Fig. 4.14c. Therefore, we define the fully superconducting range ($T < 6$K), the transition temperature range ($6\text{K} < T < 9\text{K}$), and the normal state range ($9\text{K} < T$).

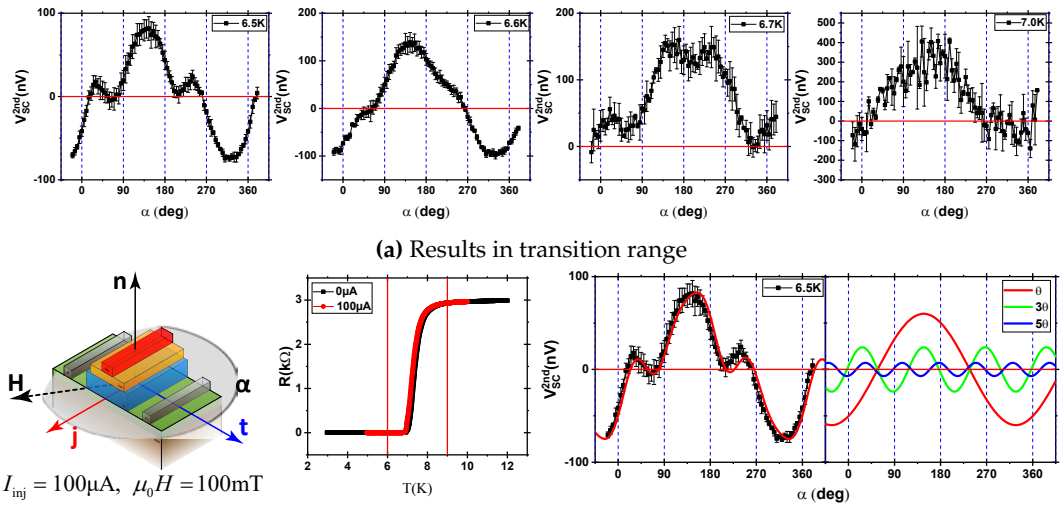

(a) Results in transition range

(b) Experimental setup **(c)** T_c **(d)** Experimental setup

Figure 4.14: Results from the structure with a 12nm NbN strip: (a) The results at the temperature (6.5K, 6.6K, 6.7K and 7.0K); The angular dependence of the 2nd signals are different from a cosine shape at 6.5K, 6.6K, and 6.7K, while it is back to a cosine shape at 7.0K. (b) Experimental setup; We drive 100µA charge current with an AC source through the top heater when rotating the external magnetic field in-plane. (c) T_c measurement of the 12nm NbN strip using the 4-point method; (d) FFT results of the result at 6.5K; There exist signals with other periodicities (360°, 120°, and 72°)

Results Focusing on the results in the transition range shown in Fig. 4.14a, the angular dependence of the 2nd harmonic signals is not in a cosine shape at $T = 6.5$ K at the start of

the transition range. With increasing temperature, the shape eloves into the cosine shape with phase shift and offset, which we found in previous sections. We perform a fast Fourier transformation (FFT) on the results at 6.5K, shown in Fig.4.14d. The FFT gives the magnitude of the the each term and the signal of $6.5\,\mathrm{K}$ has three peaks at the 1^{st}, 3^{rd}, and 5^{th} term. The signal is a sum of the 1^{st}, 3^{rd}, and 5^{th} terms of Fourier series, whose corresponding amplitudes are 60nV, 22nV and 7nV. Unfortunately, there exist phases on all three terms which are neither 90° nor 180°. The phase in the 1^{st} term is the same (about 30°) as the phase shift of the signals at a higher temperature. We assume that the amplitudes of higher terms decrease with increasing temperature. The first term may contribute to the phase shift.

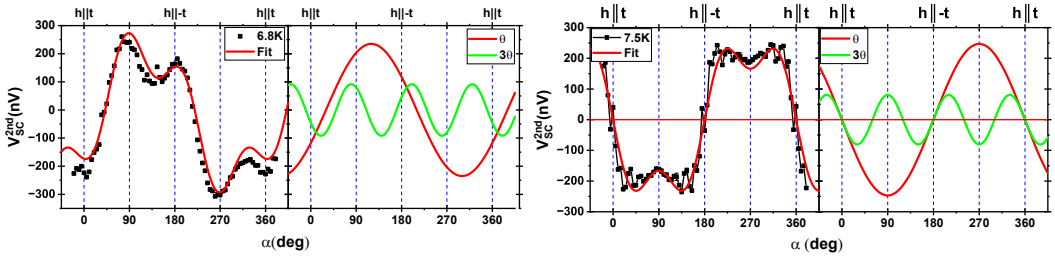

(a) Results in IP geometry

(b) Results in OOPJ geometry

Figure 4.15: FFT results of IP and OOPJ geometry: (a) FTT results when rotating magnetic field in IP geometry; The results are from Fig.4.6. We drive a 100µA injection current through the side heater with a 500mT magnitude of the external magnetic field in IP geometry. (b) FTT results when rotating magnetic field in OOPJ geometry; We drive a 100µA injection current through the side heater with a 100mT magnitude of the external magnetic field in OOPJ geometry.

Next, we focus on other results from the previous section shown in Fig.4.15. In Fig.4.15a, we present the FFT results of the data from Fig.4.6. We drive a 100µA injection current through the side heater with a 500mT magnitude of the external magnetic field in IP geometry. As is discussed in Sec.4.1.3, the amplitude of higher terms increases with the increasing magnitude of the external magnetic field. Moreover, Fig.4.15b shows the FTT results on the data when rotating the external magnetic field in OOPJ geometry. It shows that the signals when the magnetic field is rotated in OOPJ geometry consist of a $\sin\theta$ signal and a $\sin 3\theta$ signal without phase shift. It illustrates that the OOP component of the magnetic field might give rise to the signals with other periods. Furthermore, there exist no differences between the results when the external magnetic field is rotated in OOPJ and OOPT geometry discussed in Sec.4.1.3, which indicates that the IP component of the external magnetic field does not play a role in experiments when the magnetic field is rotated in OOPJ or OOPT geometry. Therefore, we infer that the OOP component of the external magnetic field might give rise to the signals with other periodicities.

Furthermore, there exist several mechanisms that might give rise to the signals with different periodicities. The spin transport process includes the generation of the spin current, the conversion of the spin current and the charge current, and the detection of the voltage signals due to the charge accumulation. First, apart from the spin current generated via the SSE, there might exist other spin currents generated via the spin Nernst effect. The spin Nernst effect is a phenomenon of spin separation caused by the thermal flow of electrons in condensed matter. According to the report [69, 70], the angular dependence of the SNE

is $\sin^2(\theta)$ or $\sin(2\theta)$, so it might not be the origin of the $\sin(3\theta)$ term. However, under our experimental setup, we should not detect such large SNE signals. Next, there might exist other spin transport mechanisms in SC. Not only the electrons and QPs but also the vortices in SC can carry spins [66, 71]. The spin-charge conversion of the spin currents carried by vortices might perform different angular dependence on the external magnetic field and therefore give rise to signals with other periodicities. Moverover, the signals with other periodicities might originate from higher-even harmonic signals using the AC lock-in technique. As is shown in Eq.(9), the second harmonic signal $V^{2\omega}$ represents effects that are even under current reversal and is governed by R_2, R_4, and higher even number coefficients. The mechanism related to the higher even number coefficients might contribute to the additional signals with other periodicities.

4.3 Control measurements on a reference sample

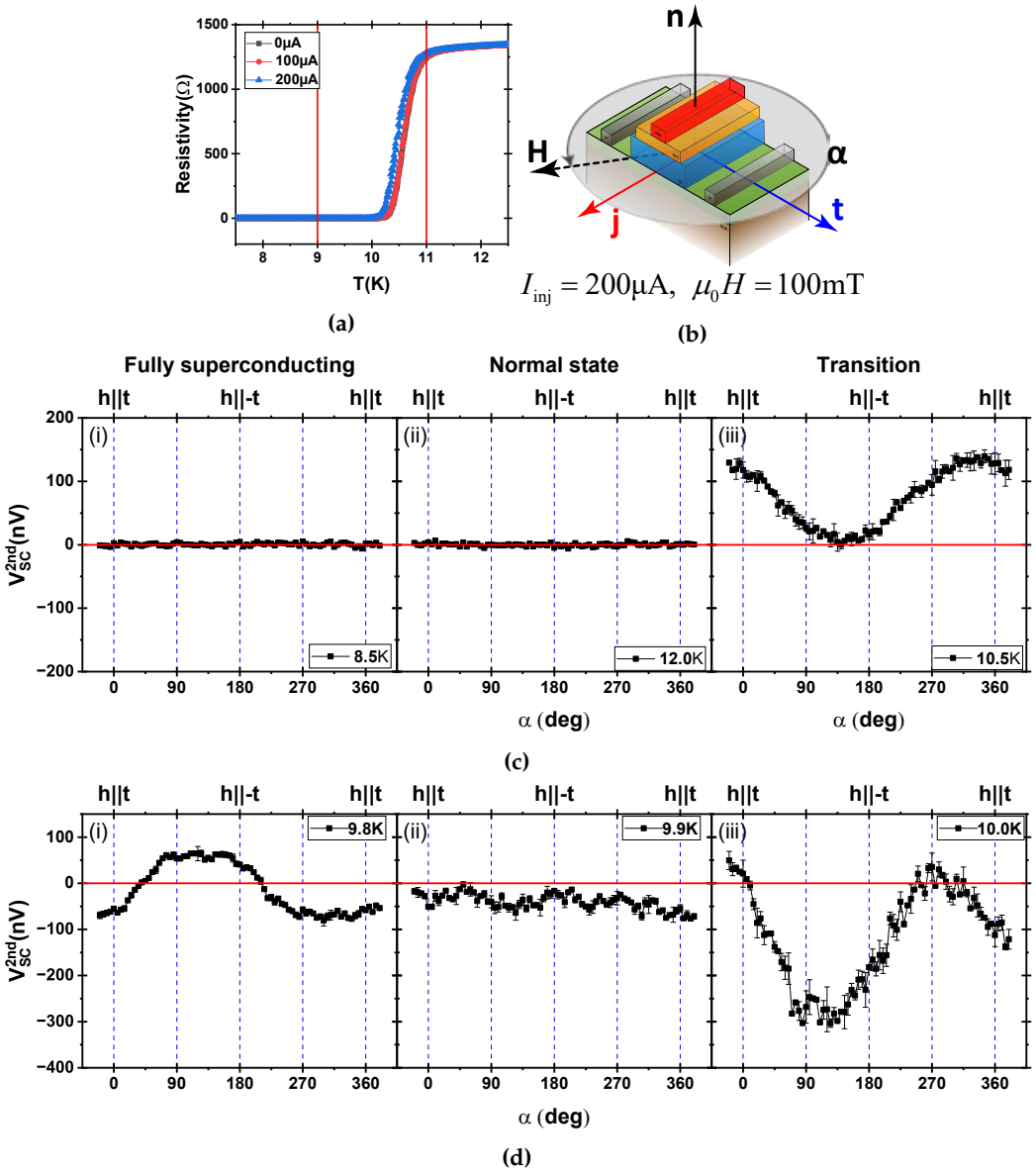

Figure 4.16: The results from the structure on a silicon substrate. (a) $T_c = 10.5K$ of the central NbN strip; (b) The experimental setup; We apply a 7.737Hz sinusoidal wave with an amplitude of 200μA on the top heater and rotate the external magnetic field with a magnitude of 100mT in the $j-t$ plane. (c) $V_{\mathrm{SC}}^{2\mathrm{nd}}(\alpha)$ at 8.5K, 10.5K, and 12K. We detect no signals in the fully superconducting range and the normal state range; A cosine shape signal with phase shift and offset is detected in the transition range. (d) The behavior of the sign-change in the transition range.

In this section, we introduce the results of the ADMR measurements from the structure patterned on a silicon substrate. The layout of the structure is the same as the structure introduced in Sec. 3.1. We repeat the IP-ADMR measurements on this structure. We drive an injection charge current on the top heater with an AC source and detect the corresponding voltage signal with a lock-in amplifier. The external magnetic field is rotated in the IP geometry. Surprisingly, we detect signals which exhibit the same behavior as the results in previous sections. The T_c of the NbN, shown in Fig. 4.16a, is around 10.5K. From this, we define the fully superconducting range ($T < 9\mathrm{K}$), the transition range ($9\mathrm{K} < T < 11\mathrm{K}$),

and the normal state range ($11\text{K} < T$).

Fig. 4.16c shows the angular dependence of the 2^{nd} harmonic signals in the fully superconducting range, the transition range, and the normal state range. We apply a 7.737Hz sinusoidal wave with an amplitude of 200µA on the top heater and rotate the external magnetic field with a magnitude of 100mT in the $j - t$ plane, shown in Fig.4.16b. We detect no signals in the fully superconducting range and the normal state range. The signals at temperatures in the transition range exhibit a cosine shape signal with a phase shift (around 30°) and a large offset, the magnitude of which is comparable to its amplitude. Moreover, in the transition range shown in Fig. 4.16d, we find a gradual change of the sign of cosine-shaped 2nd Harmonic response. To further illustrate the behaviors of the 2^{nd} harmonic signal in the transition temperature range, we do the same modified cosine function fit on every $V_{\text{SC}}^{2\text{nd}}(\alpha)$ curve using Eq. 11.

Current dpendence The temperature dependence of three fitting parameters $A_{\text{Sc}}^{2\text{nd}}(T)$, $x_c(T)$, and $y_0(T)$ with different amplitude of the injection current are presented in Fig.4.17.

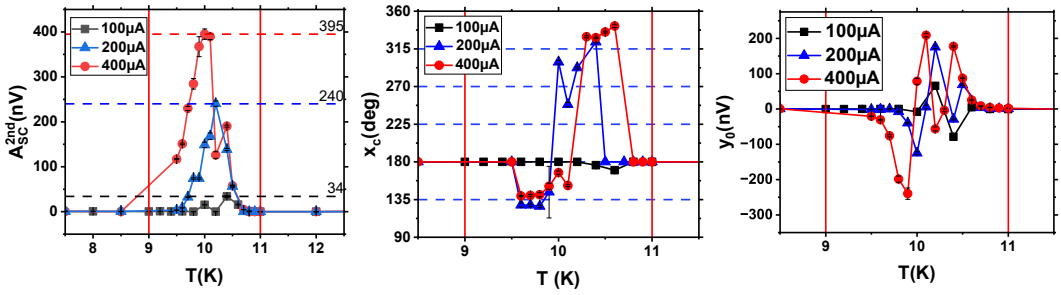

(a) Amplitude $A(T)$ **(b)** Angle shift $x_c(T)$ **(c)** Offset $y_0(T)$

Figure 4.17: Temperature dependence of the fitting parameter. When applying 100µA, 200µA, and 400µA injection current on the top heater. (a) Temperature dependence of the amplitude; The amplitude of the signals increases with the increasing magnitude of the applied charge currents. (b) Temperature dependence of the phase shift; There is a phase change about 30°. (c) The temperature dependence of the offset; The offset of the signals also increases with the increasing magnitude of the applied charge currents.

As there is no spin transport across the Si/SC interface, the signals at the temperature in the transition must originate from other mechanisms. These results are likely related to the phenomenon in the superconducting NbN strip or at the interface between the superconductor NbN and the connection pads made of normal metal (Pt or Al). Therefore there might exist other spin currents which are not driven via the SSE. These unexpected spin currents might contribute to the angle shift and the offset in the thermopower signal measurements presented in the previous section.

5 Summary and outlook

In this chapter, a brief summary of the results of this thesis as well as an outlook for further research is given.

5.1 Summary

In this thesis, we investigate the QP-mediated spin transport at NbN/YIG interface via the SSE. To this end, we pattern three-terminal structures on a YIG substrate and deposit the material with the magnetron sputtering technique. We have performed the AMDR measurements on the structure to investigate the thermal voltage signals and detect the signals using AC lock-in technology, which is explained in Ch. 3.

We have performed our experiments with two different heater configurations to drive temperature gradients. The results, when using the side heaters and thus making the temperature of the YIG layer higher than the one of the superconductor, are presented in Sec. 4.1, and the results when using the top heater in Sec. 4.2. Moreover, the results from structures fabricated on a silicon substrate are shown in Sec. **??**. The thermopower signals exhibit a richer behavior than expected. To characterize the angular dependence of thermopower signals on the external magnetic field, we have performed a modified cosine function fitting with a fitting function Eq. (11). From this approach we extract the following interesting results:

Signals enhancement near T_c As is shown in Fig. 4.3a and Fig. 4.11a, we detect no signals when the NbN stripe is fully superconducting and only a small SSE signal when the NbN stripe is in the normal state. The amplitude of the thermopower signals around T_c from our structure is enhanced three or four times with respect to the signals in the normal state, compared to the results reported by Jeon et al. [6], where a signal enhancement up to three orders of magnitude is observed. The short coherence length of the NbN ($\simeq$ 5 nm), which as compared to Nb [6], contributes to this difference. The amplitude increases with the increasing current as shown in Fig. 4.5a and Fig. 4.11a because the large heating current leads to large heating power and hence large temperature gradients. Moreover, we detect larger signals from thinner NbN strips, as is shown in Fig. 4.7, which is in agreement with the work by Jeon et al [6].

Phase shift around T_c We detect a shift in the angle position of the cosine-shaped $V_{\mathrm{SC}}^{\mathrm{2nd}}(\alpha)$-curve near T_c and no shift when NbN strips are in the normal state, as is shown in Fig. 4.2 and Fig. 4.11. The amplitude of the injection charge current does not affect the shift as is shown in Fig. 4.5b. The shift changes on the structures with different thicknesses of the central NbN strip, as shown in Fig. 4.7. For the structures fabricated on different chips, we cannot infer that the shift is related to the thickness of the central NbN strip.

Large offset signal around T_c We detect a large offset contribution to the $V_{\mathrm{SC}}^{\mathrm{2nd}}(\alpha)$ curve near T_c and no offset when NbN strips are in the normal state, as is shown in Fig. 4.3c and Fig. 4.11c. The offset increase with the increasing amplitude of the injection charge

currents, as is shown in Fig. 4.5c. Moreover, we detect a larger offset on the structure with a thinner central NbN strip in Fig. 4.7.

Several sign-changes of the thermopower signals As is shown in Fig. 4.2 and Fig. 4.11, we find several sign-changes of the amplitude of the cosine-shaped thermopower signals near T_c. These sign-changes are visible as the 180° rapid changes in the $x_c(T)$ curve in Fig. 4.3c and Fig. 4.11c.

Resistance change when rotating the external magnetic field When rotating the external magnetic field in different rotation planes, we observe that the resistance of the central NbN strip changes with the orientation of the external magnetic field as is shown in Fig. 4.13. For the results when the magnetic field is rotated in the OOPJ geometry, the resistance change originates from the fact that the OOP component of the magnetic field will induce resistive vortices in the NbN strip. Interestingly, when rotating the magnetic field in IP geometry, the $R(\alpha)$ curve shows a cosine shape with the maximum located at 60 °. The position of the maximum of the $R(\alpha)$ curve corresponds to the shift in the cosine-shaped thermopower signals near T_c. Thus, the resistance change might be related to the phase shift of the SSE signals.

Results when rotating magnetic field in OOPJ and OOPT geometry We perform the same ADMR measurements when rotating the external magnetic field in OOPJ and OOPT geometry, the thermopower signals behave differently compared to the results from the reference Pt strip in Fig. 4.4. The signals change their sign when the external magnetic field is perpendicular to the normal direction of the YIG substrate and exhibit no difference when the magnetic field is rotated in OOPJ and OOPT geometry. It indicates that the OOP component of the magnetic field dominates the thermopower signal and also indicates that the OOP component of the magnetic potentially contributes to the shift in the angle-position of the thermopower signals when the magnetic field is rotated in the IP geometry.

Rise of signals with other periodicities To better characterize the $V_{\mathrm{SC}}^{\mathrm{2nd}}(\alpha)$ curve, which is not in a cosine shape in Fig. 4.14 and 4.6, we perform an FFT analysis on these results. Furthermore, in Fig. 4.15 and Fig.4.14, there exist large signals of $\cos 3\theta$ term in fit results. As is shown in Fig. 4.15a, there exists a difference in x_c between the $\cos\theta$ term and the $\cos 3\theta$ term. Since the signals evolve into a cosine shape when the temperature increases in Fig. 4.6, the signals of 3θ term decrease with increasing temperature. Moreover, as shown in Fig. 4.15b, the signals when the external magnetic field is rotated in OOPJ geometry also consist of the signals with different periodicities, which indicates that the signals with other periodicities originate from the OOP component of the external magnetic field.

Moreover, we also perform ADMR measurements on a reference structure fabricated on a silicon substrate. Although we expect no SSE signals, we detect some thermovoltage signals near T_c as is shown in Fig. 4.16. It indicates that there exist mechanisms contributing to the detected voltage signal in IP geometry besides the SSE.

5.2 Outlook

The thermopower signals around T_c exhibit a richer behavior than expected. Other than the enhancement of the thermopower signals near T_c, we also observe other behaviors such as a phase shift in angle position, an offset, and several sign changes. It indicates that another mechanism contributes to the detected thermovoltage signal, which may not only originate from the SC/FMI interface. The most interesting part is the shift in the angle position of thermopower signals near T_c. One of the goals of further investigations is to try to control the phase shift of the thermovoltage signal signals. First, we should find out the parameters that can affect these behaviors. We can use more different amplitudes of the injection current and the magnitudes of the external magnetic field. Moreover, we can try to perform the ADMR measurements with a very small magnitude of the external magnetic field such as 20mT. Next, We should try to fabricate the structures with different thicknesses of the central NbN strip on the same chip in order to find out the thickness dependence of the phase shift. Furthermore, as these rich behaviors might be related to the vortices in the superconductor, we should find ways to control the vortices to investigate the relationships between the SSE signals and the vortices. We can also try to fabricate the structure with higher quality, try to improve the superconductivity of the central superconducting strip, and use a thinner YIG film deposited via pulsed laser deposition.

A Appendix

A.1 Lithography in *NanoBeam nB5*

An example of the file of the writting process

```
# run nbwrite YS/20220809-YIG-G-SC -1=ys:alignemento1 -2=ys:alignementp1
# focusmap

#------------------------------------------------------------
.global
registration    (0,2 300 000) (5 000 000, 2 300 000)
registration    (0,         0) (5 000 000,         0)
marktype                    mp_sqr10
focus                       map1
.end

#------------------------------------------------------------
.block
focus                       global_map
stepsize                    (0,0)
grid                        (1,1)
base_dose                   2.0
pattern                     yagpt    (- 250 000,- 1 100 000)
.end

#------------------------------------------------------------
.pattern
id                                  yagpt
filename                    YS/20220809-YIG-G-SC.npf
dose    2   1.5
.end

#------------------------------------------------------------
.write
current                     auto
mf_trim                     (1.0001, 1.0001, 0, 0)
sf_trim                     (1.001, 1.001, 0, 0)
.end
```

References

[1] M. Hilbert and P. López, Science **332**, 60 (2011).

[2] H. Lasi, P. Fettke, T. Feld, and M. Hoffmann, Business & Information Systems Engineering **6**, 239 (2014).

[3] G. E. Moore, IEEE J. **11**, 33 (2006).

[4] M. M. Waldrop, Nature News **530**, 144 (2016).

[5] J. Linder and J. W. A. Robinson, Nat. Phys. **11**, 307 (2015).

[6] K.-R. Jeon, J.-C. Jeon, X. Zhou, A. Migliorini, J. Yoon, and S. S. P. Parkin, ACS Nano **14**, 15874 (2020).

[7] T. Wakamura, H. Akaike, Y. Omori, Y. Niimi, S. Takahashi, A. Fujimaki, S. Maekawa, and Y. Otani, Nat. Mater. **14**, 675 (2015).

[8] J. Xiao, G. E. W. Bauer, K.-c. Uchida, E. Saitoh, and S. Maekawa, Phys. Rev. B **81**, 214418 (2010).

[9] J. Shan, L. J. Cornelissen, N. Vlietstra, J. Ben Youssef, T. Kuschel, R. A. Duine, and B. J. van Wees, Phys. Rev. B **94**, 174437 (2016).

[10] J. E. Hirsch, Phys. Rev. Lett. **83**, 1834 (1999).

[11] E. Saitoh, M. Ueda, H. Miyajima, and G. Tatara, Appl. Phys. Lett. **88**, 182509 (2006).

[12] K. Ganzhorn, T. Wimmer, J. Cramer, R. Schlitz, S. Geprägs, G. Jakob, R. Gross, H. Huebl, M. Kläui, and S. T. B. Goennenwein, AIP. ADV. **7**, 085102 (2017).

[13] S. Takahashi and S. Maekawa, Jpn. J. Appl. Phys. **51**, 010110 (2011).

[14] T. Kato, Y. Ohnuma, M. Matsuo, J. Rech, T. Jonckheere, and T. Martin, Phys. Rev. B **99**, 144411 (2019).

[15] T. Wimmer, *Spin Transport in Magnetic Nanostructures*, Master's thesis, Technische Universität München (2016).

[16] M. V. Berry, Proc. R. Soc. Lond.A **392**, 45 (1984).

[17] J. Smit, Physica **24**, 39 (1958).

[18] L. Berger, Phys. Rev. B **2**, 4559 (1970).

[19] M. Evelt, L. Soumah, A. Rinkevich, S. Demokritov, A. Anane, V. Cros, J. Ben Youssef, G. de Loubens, O. Klein, P. Bortolotti, and V. Demidov, Phys. Rev. Appl. **10**, 041002 (2018).

[20] A. Hamadeh, O. d'Allivy Kelly, C. Hahn, H. Meley, R. Bernard, A. H. Molpeceres, V. V. Naletov, M. Viret, A. Anane, V. Cros, S. O. Demokritov, J. L. Prieto, M. Muñoz, G. de Loubens, and O. Klein, Phys. Rev. Lett. **113**, 197203 (2014).

[21] M. Collet, X. de Milly, O. d'Allivy Kelly, V. V. Naletov, R. Bernard, P. Bortolotti, J. Ben Youssef, V. E. Demidov, S. O. Demokritov, J. L. Prieto, M. Muñoz, V. Cros, A. Anane, G. de Loubens, and O. Klein, Nat. Commun. **7**, 10377 (2016).

[22] M. Evelt, V. E. Demidov, V. Bessonov, S. O. Demokritov, J. L. Prieto, M. Muñoz, J. Ben Youssef, V. V. Naletov, G. de Loubens, O. Klein, M. Collet, K. Garcia-Hernandez, P. Bortolotti, V. Cros, and A. Anane, Appl. Phys. Lett. **108**, 172406 (2016).

[23] A. Hoffmann, IEEE Trans. Magn. **49**, 5172 (2013).

[24] L. Liu, C.-F. Pai, Y. Li, H. W. Tseng, D. C. Ralph, and R. A. Buhrman, Science **336**, 555 (2012).

[25] M. Schreier, G. E. W. Bauer, V. I. Vasyuchka, J. Flipse, K.-i. Uchida, J. Lotze, V. Lauer, A. V. Chumak, A. A. Serga, S. Daimon, T. Kikkawa, E. Saitoh, B. J. van Wees, B. Hillebrands, R. Gross, and S. T. B. Goennenwein, J. Phys. D: Appl. Phys. **48**, 025001 (2014).

[26] L. J. Cornelissen, J. Liu, R. A. Duine, J. B. Youssef, and B. J. van Wees, Nat.Phys. **11**, 1022 (2015).

[27] A. Kehlberger, U. Ritzmann, D. Hinzke, E.-J. Guo, J. Cramer, G. Jakob, M. C. Onbasli, D. H. Kim, C. A. Ross, M. B. Jungfleisch, B. Hillebrands, U. Nowak, and M. Kläui, Phys. Rev. Lett. **115**, 096602 (2015).

[28] M. Schreier, N. Roschewsky, E. Dobler, S. Meyer, H. Huebl, R. Gross, and S. T. B. Goennenwein, Appl. Phys. Lett. **103**, 242404 (2013).

[29] E.-J. Guo, J. Cramer, A. Kehlberger, C. A. Ferguson, D. A. MacLaren, G. Jakob, and M. Kläui, Phys. Rev. X **6**, 031012 (2016).

[30] A. Khitun, M. Bao, and K. L. Wang, J. Phys. D: Appl. Phys. **43**, 264005 (2010).

[31] A. V. Chumak, A. A. Serga, and B. Hillebrands, Nat Commun **5**, 4700 (2014).

[32] S. T. B. Goennenwein, R. Schlitz, M. Pernpeintner, K. Ganzhorn, M. Althammer, R. Gross, and H. Huebl, Appl. Phys. Lett. **107**, 172405 (2015).

[33] K.-i. Uchida, H. Adachi, T. Ota, H. Nakayama, S. Maekawa, and E. Saitoh, Appl. Phys. Lett. **97**, 172505 (2010).

[34] K. Ganzhorn, S. Klingler, T. Wimmer, S. Geprägs, R. Gross, H. Huebl, and S. T. B. Goennenwein, Appl. Phys. Lett. **109**, 022405 (2016).

[35] L. J. Cornelissen, J. Shan, and B. J. van Wees, Phys. Rev. B **94**, 180402 (2016).

[36] L. J. Cornelissen, K. J. H. Peters, G. E. W. Bauer, R. A. Duine, and B. J. van Wees, Phys. Rev. B **94**, 014412 (2016).

[37] M. Schreier, A. Kamra, M. Weiler, J. Xiao, G. E. W. Bauer, R. Gross, and S. T. B. Goennenwein, Phys. Rev. B **88**, 094410 (2013).

[38] S. A. Kivelson and D. S. Rokhsar, Phys. Rev. B **41**, 11693 (1990).

[39] H. L. Zhao and S. Hershfield, Phys. Rev. B **52**, 3632 (1995).

[40] F. S. Bergeret, M. Silaev, P. Virtanen, and T. T. Heikkilä, Rev. Mod. Phys. **90**, 041001 (2018).

[41] T. Yamashita, S. Takahashi, H. Imamura, and S. Maekawa, Phys. Rev. B **65**, 172509 (2002).

[42] S. Takahashi and S. Maekawa, Phys. Rev. B **67**, 052409 (2003).

[43] J. P. Morten, A. Brataas, and W. Belzig, Phys. Rev. B **70**, 212508 (2004).

[44] J. P. Morten, A. Brataas, and W. Belzig, Phys. Rev. B **72**, 014510 (2005).

[45] M. Silaev, P. Virtanen, F. S. Bergeret, and T. T. Heikkilä, Phys. Rev. Lett. **114**, 167002 (2015).

[46] F. Aikebaier, M. A. Silaev, and T. T. Heikkilä, Phys. Rev. B **98**, 024516 (2018).

[47] S. Takahashi and S. Maekawa, J. Phys. Soc. Jpn. **77**, 031009 (2008).

[48] S. Takahashi and S. Maekawa, Phys. Rev. Lett. **88**, 116601 (2002).

[49] H. Kontani, J. Goryo, and D. S. Hirashima, Phys. Rev. Lett. **102**, 086602 (2009).

[50] G. Yang, C. Ciccarelli, and J. W. A. Robinson, APL Materials **9**, 050703 (2021).

[51] J. R. Schrieffer, J. Supercond. **4**, 317 (1991).

[52] P. Coleman, E. Miranda, and A. Tsvelik, Phys. Rev. B **49**, 8955 (1994).

[53] E. Abrahams, A. Balatsky, D. J. Scalapino, and J. R. Schrieffer, Phys. Rev. B **52**, 1271 (1995).

[54] M. Eschrig, Phys. Today **64**, 43 (2011).

[55] M. Müller, L. Liensberger, L. Flacke, H. Huebl, A. Kamra, W. Belzig, R. Gross, M. Weiler, and M. Althammer, Phys. Rev. Lett. **126**, 087201 (2021).

[56] G. Terrasanta, M. Müller, T. Sommer, S. Geprägs, R. Gross, M. Althammer, and M. Poot, Mater. Quantum. Technol. **1**, 021002 (2021).

[57] *Sputtering by Particle Bombardment*, Topics in Applied Physics, Vol. 110 (Springer, Berlin, Heidelberg, 2007).

[58] M. Manuel, *Superconductor/Ferromagnet Heterostructures for Superconducting Spintronics*, Master's thesis, Technische Universität München (2020).

[59] J. H. Scofield, American Journal of Physics **62**, 129 (1994).

[60] M. Inoue, M. Ichioka, and H. Adachi, Phys. Rev. B **96**, 024414 (2017).

[61] Y. Yao, Q. Song, Y. Takamura, J. P. Cascales, W. Yuan, Y. Ma, Y. Yun, X. C. Xie, J. S. Moodera, and W. Han, Phys. Rev. B **97**, 224414 (2018).

[62] M. Umeda, Y. Shiomi, T. Kikkawa, T. Niizeki, J. Lustikova, S. Takahashi, and E. Saitoh, Appl. Phys. Lett. **112**, 232601 (2018).

[63] D. Beckmann, J. Phys.: Condens. Matter **28**, 163001 (2016).

[64] T. Matsushita, J. Ando, Y. Masaki, T. Mizushima, S. Fujimoto, and I. Vekhter, Phys. Rev. Lett. **128**, 097001 (2022).

[65] Y. Shiomi, J. Lustikova, and E. Saitoh, Sci. Rep. **7**, 5358 (2017).

[66] S. K. Kim, R. Myers, and Y. Tserkovnyak, Phys. Rev. Lett. **121**, 187203 (2018).

[67] N. Vlietstra, J. Shan, V. Castel, B. J. van Wees, and J. Ben Youssef, Phys. Rev. B **87**, 184421 (2013).

[68] P. Sheng, Y. Sakuraba, Y.-C. Lau, S. Takahashi, S. Mitani, and M. Hayashi, Science Advances **3**, e1701503 (2017).

[69] S. Meyer, Y.-T. Chen, S. Wimmer, M. Althammer, T. Wimmer, R. Schlitz, S. Geprägs, H. Huebl, D. Ködderitzsch, H. Ebert, G. E. W. Bauer, R. Gross, and S. T. B. Goennenwein, Nat. Mater. **16**, 977 (2017).

[70] T. Wimmer, J. Gückelhorn, S. Wimmer, S. Mankovsky, H. Ebert, M. Opel, S. Geprägs, R. Gross, H. Huebl, and M. Althammer, Phys. Rev. B **104**, L140404 (2021).

[71] T. Taira, Y. Kato, M. Ichioka, and H. Adachi, Phys. Rev. B **103**, 134417 (2021).

B Acknowledgments

In the last year, finishing my master thesis work at the Walther-Meißner Institut (WMI) was quite a pleasant experience. Here, I really thank everybody at the WMI for helping me finish my work. In particular, I would like to thank:

Prof. Dr. Rudolf Gross for giving me the opportunity to write my master's thesis at the WMI.

Dr. Matthias Althammer as my advisor, for instructing me to perform my measurements. The instruction you give me helped me a lot to find the direction of the next step of measurements. Thank you for the discussions which helped me to fully understand the physics behind the measurements.

Manuel Müller for instructing me to operate the devices in the lab, including the Superbowl system and the Chaos cryostat system. Moreover, either physics or non-physics related discussions helped me a lot.

Janine Gückelhorn for the help you gave me in the operation of the e-beam lithography devices. Moreover, I would like to thank you for the instruction on the AC lock-in detection technique.

Last but definitely not least my family, especially my parents, for always supporting me emotionally and financially, as well as encouraging me to follow my dreams and passion. I am very grateful for enabling me to study at the TU-Munich.